Basinwide Integrated Volume Transports in an Eddy-Filled Ocean

T. KANZOW

Ozeanzirkulation und Klimadynamik, Leibniz-Institut für Meereswissenschaften an der Universität Kiel, Kiel, Germany, and Ocean Observing and Climate Research Group, National Oceanography Centre, Southampton, Southampton, United Kingdom

H. L. JOHNSON

Department of Earth Sciences, University of Oxford, Oxford, United Kingdom

D. P. MARSHALL

Atmospheric, Oceanic and Planetary Physics, Clarendon Laboratory, University of Oxford, Oxford, United Kingdom

S. A. CUNNINGHAM, J. J.-M. HIRSCHI, A. MUJAHID, AND H. L. BRYDEN

Ocean Observing and Climate Research Group, National Oceanography Centre, Southampton, Southampton, United Kingdom

W. E. JOHNS

Division of Meteorology and Physical Oceanography, Rosenstiel School of Marine and Atmospheric Science, Miami, Florida

(Manuscript received 14 November 2008, in final form 16 June 2009)

ABSTRACT

The temporal evolution of the strength of the Atlantic Meridional Overturning Circulation (AMOC) in the subtropical North Atlantic is affected by both remotely forced, basin-scale meridionally coherent, climate-relevant transport anomalies, such as changes in high-latitude deep water formation rates, and locally forced transport anomalies, such as eddies or Rossby waves, possibly associated with small meridional coherence scales, which can be considered as noise. The focus of this paper is on the extent to which local eddies and Rossby waves when impinging on the western boundary of the Atlantic affect the temporal variability of the AMOC at 26.5°N. Continuous estimates of the AMOC at this latitude have been made since April 2004 by combining the Florida Current, Ekman, and midocean transports with the latter obtained from continuous density measurements between the coasts of the Bahamas and Morocco, representing, respectively, the western and eastern boundaries of the Atlantic at this latitude.

Within 100 km of the western boundary there is a threefold decrease in sea surface height variability toward the boundary, observed in both dynamic heights from in situ density measurements and altimetric heights. As a consequence, the basinwide zonally integrated upper midocean transport shallower than 1000 m—as observed continuously between April 2004 and October 2006—varies by only 3.0 Sv (1 Sv $\equiv 10^6$ m^3 s^{-1}) RMS. Instead, upper midocean transports integrated from western boundary stations 16, 40, and 500 km offshore to the eastern boundary vary by 3.6, 6.0, and 10.7 Sv RMS, respectively.

The reduction in eddy energy toward the western boundary is reproduced in a nonlinear reduced-gravity model suggesting that boundary-trapped waves may account for the observed decline in variability in the coastal zone because they provide a mechanism for the fast equatorward export of transport anomalies associated with eddies impinging on the western boundary. An analytical model of linear Rossby waves suggests a simple scaling for the reduction in thermocline thickness variability toward the boundary. Physically, the reduction in amplitude is understood as along-boundary pressure gradients accelerating the fluid and rapidly propagating pressure anomalies along the boundary. The results suggest that the local eddy field does not dominate upper midocean transport or AMOC variability at 26.5°N on interannual to decadal time scales.

Corresponding author address: T. Kanzow, Ozeanzirkulation und Klimadynamik, Leibniz-Institut für Meereswissenschaften, Universität Kiel, Düsternbrooker Weg 20, 24105 Kiel, Germany.
E-mail: tkanzow@ifm-geomar.de

DOI: 10.1175/2009JPO4185.1

1. Introduction

Observational studies targeting large-scale circulation changes have relied on ''endpoint'' measurement techniques to provide estimates of the net transport across vertical sections (e.g., Whitworth 1983; McPhaden and Zhang 2002; Johns et al. 2005; Kanzow et al. 2006). The large-scale flow in the ocean interior is in geostrophic balance to first order (away from the surface and bottom Ekman layers), and endpoint vertical density profiles can be used to compute the net geostrophic flow (relative to a level of reference) between them. The absolute geostrophic horizontal velocity $\mathbf{U} = (u, v)$ can be deduced from the horizontal gradient in pressure P in the ocean, according to

$$2\boldsymbol{\Omega} \times \mathbf{U} = \frac{1}{\rho}\nabla_H P, \tag{1}$$

with $\boldsymbol{\Omega}$ and ρ denoting the earth's angular velocity and reference ocean density, respectively. On a zonal section, the Coriolis parameter f is constant and the horizontal pressure difference between the eastern and western endpoints (P_E, P_W) is proportional to the zonally integrated northward geostrophic volume transport per unit depth, T:

$$T(t, z) = \frac{[P_E(t, z) - P_W(t, z)]}{\rho f}, \tag{2}$$

with z and t denoting depth and time, respectively.

The pressure at $z = -h$ can be written as the displacement of sea level from its time mean η and the density of the water column,

$$P(t, -h) = \rho_0 g\eta(t) - \int_{-h}^{0} \rho(t, z) g\, dz, \tag{3}$$

where g is the earth's gravitational acceleration. It is assumed that an inverted barometer correction has been applied to η, at a rate of $\Delta P_A(t) = g\rho_0\Delta\eta(t)$ (e.g., Fu and Pihos 1994), so dynamically inactive changes ($\Delta\eta$) due to deviations in atmospheric pressure from the long-term mean (ΔP_A) are removed. The geostrophic balance is a valid approximation even in the strongest (fastest) ocean current systems, such as the Antarctic Circumpolar Current (ACC; Whitworth 1983), the Gulf Stream (Sato and Rossby 1995), the Kuroshio (Johns et al. 2001), the Agulhas Current (Beal and Bryden 1999), or the Atlantic deep western boundary current (DWBC; Johns et al. 2005).

Recently, the endpoint measurement technique has been used to infer meridional transport variations across a 6000-km transatlantic section between the Bahamas and the Moroccan coast at 26.5°N in the Atlantic (Fig. 1; Cunningham et al. 2007; Kanzow et al. 2007), hereafter referred to as midocean transport. Cunningham et al. (2007) show that the daily upper midocean transport shallower than approximately 1000 m displays fluctuations of 3.1 Sv (1 Sv $\equiv 10^6$ m^3 s^{-1}) RMS for the period between April 2004 and April 2005. As a consequence of the westward energy transfer effected by Rossby waves and eddies and of instabilities in the boundary current systems, significantly elevated levels of surface eddy kinetic energy are commonly found near the western boundaries of the ocean (see Fig. 9b in Wunsch and Stammer 1998). Using mooring-based observations of upper-ocean transports across 26.5°N, we investigate how eddy variability[1] within 500 km of the western boundary affects basinwide integrated transports. This question is important for the interpretation of the variability of both the Atlantic Meridional Overturning Circulation (AMOC) and the subtropical gyre at this latitude. Important currents in the western boundary region here include the southward-flowing DWBC below 1000 m and the northward-flowing Antilles Current in the upper 1000 m (Lee et al. 1990, 1996; Bryden et al. 2005; Johns et al. 2008).

Transient eddy variability is sometimes important for the horizontal redistribution of heat, salt, and momentum but may be a source of noise in experiments aimed at characterizing the temporal evolution of the large-scale ocean circulation using endpoint methods (e.g., Kanzow et al. 2008a). An eddy's rotation-related maximum pressure anomaly is located at its center so that the rotational transport is largest when integrating over its radius. Integrating over the eddy's diameter, the rotational transport cancels. Thus, if the eddy's horizontal extent is fully contained within the section when passing across it, only the across-section eddy translation but not its rotational flow has an impact on net across-section transports. Conversely, eddies passing over one endpoint contribute to fluctuations in the net zonal pressure gradient, causing noise that has the potential to mask the temporal evolution of the pressure gradients associated with the large-scale flow field.

Altimetry might represent an efficient tool to estimate the time-variable strength of upper-ocean velocities. Transient features of geostrophic surface flow are proportional to the sea surface slope η and have been monitored by satellite altimetry. Numerous applications have been presented for the study of wind-driven gyres, mesoscale flows, and strong ocean currents (e.g., Stammer 1997; Chelton

[1] Eddy variability is a collective term in this study referring to transient eddies, Rossby waves, and recirculations of the western boundary Antilles Current.

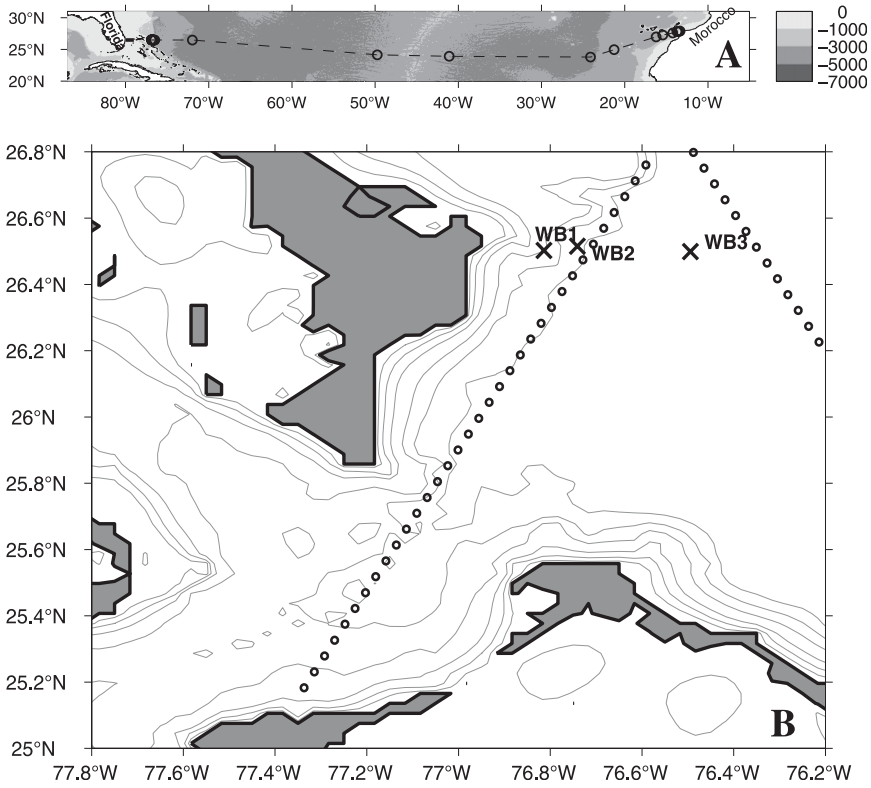

FIG. 1. (a) The distribution of moorings along 26.5°N in the subtropical North Atlantic. (b) Locations of western boundary moorings WB1–WB3 (crosses). Black dots indicate the TOPEX/Poseidon (*Jason-1*) ground track.

et al. 2007; Cunningham and Pavic 2007). The time-variable geostrophic transport T_η over the depth range $[-h, 0]$ can be estimated by associating the geostrophic surface flow with one dominant vertical mode of horizontal velocity $F(z)$ according to

$$T_\eta = [\eta_w - \eta_E] \int_{-h}^{0} F(z)\, dz. \tag{4}$$

Away from the boundaries, the upper-ocean geostrophic flow on time scales longer than a few weeks exhibits a surface-intensified first mode baroclinic structure (Wunsch 1997), whose velocity zero crossing is typically found around 1500 m. Such motions mainly reflect westward-propagating baroclinic eddies and Rossby waves, as satellite observations reveal (Chelton et al. 2007). However, approximating the vertical structure of geostrophic flow by linear baroclinic modes can fail near the sea surface. A sign of failure is that there is no sea surface temperature signal to the linear mode. Observations from the Mid-Ocean Dynamics Experiment (MODE Group 1978) showed that temperature-inferred vertical displacements do not necessarily decrease toward the sea surface (Richman et al. 1977), with the near-surface departure from linear mode theory possibly being due to shear modes (Beckmann 1988).

Barotropic motions gain in importance in the less stratified deep ocean (Wunsch 1997; Johns et al. 2005; Kanzow et al. 2008a), and from a comparison of in situ observations and altimetry in the tropical North Atlantic, Kanzow et al. (2008a) concluded that variations of η are not representative of transport changes below 1000 m.

Near boundaries, a separation of the barotropic and baroclinic modes is ambiguous because an across-boundary integral of barotropic along-boundary velocities over sloping bathymetry inevitably results in a baroclinic transport profile. Topographically trapped waves may also become important (e.g., Johns and Watts 1986) such that the relationship between η and upper-ocean transports may vary across the boundary. In addition, competing dynamics and their manifestations as vertical modes mean that a stable relationship between η and upper-ocean transports might not exist.

Using density and current meter data from the Rapid Climate Change–Meridional Overturning Circulation and Heatflux Array (RAPID–MOCHA) moorings within 500 km of the western boundary at 26.5°N, we will investigate the relationship between transports and η. In

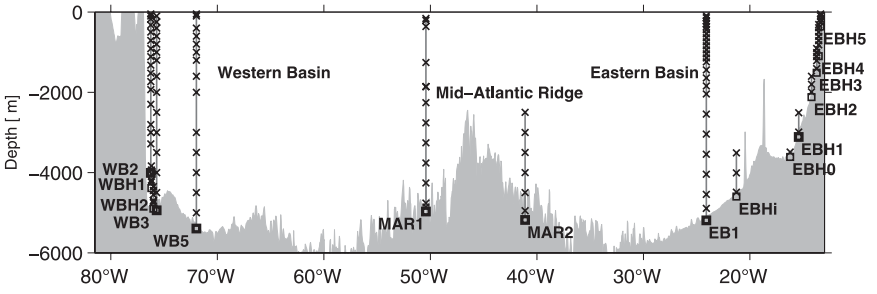

FIG. 2. Section of density (and bottom pressure) moorings along 26.5°N. The current meter moorings west of WB2 are not shown here for clarity (see Fig. 3).

particular, we test whether a robust relationship between η at the western boundary (or the boundary-to-boundary difference in η) and the upper midocean transport across 26.5°N can be established according to (4). If successful, this would enable us to estimate the strength of the AMOC at 26.5°N continuously since the launch of the Ocean Topography Experiment (TOPEX)/Poseidon altimeter in 1992 [combined with continuous estimates of the Gulf Stream and Ekman transports over this period from the Florida Current telephone cable measurements (Baringer and Larsen 2001) and wind field reanalysis products [such as those from the National Centers for Environmental Prediction–National Center for Atmospheric Research (NCEP–NCAR) reanalysis]. A stable relationship between the differences in η within a few hundred kilometers from the western boundary and η at the eastern boundary may provide a proxy for the strength of the wind-driven subtropical gyre at this latitude.

The paper is structured as follows. In section 2 we present the underlying data and methods. Section 3 describes the midocean zonally integrated transports between Morocco and four locations up to 500 km east of the Bahamas; in addition, these transports are compared with the variability in altimetric observations. In section 4 we analyze the effects of eddies impinging on the western boundary on basinwide integrated flows by means of numerical model experiments. A theoretical explanation for the model results is presented in section 5. The effects of eddies close to and at the western boundary on endpoint measurements and the implications for measuring and interpreting basinwide integrated volume transports such as the AMOC are discussed in section 6, followed by a brief summary (section 7).

2. Data and methods

a. Data

To study the influence of eddy variability on basinwide integrated transports, we derive a set of estimates of the meridional geostrophic volume transport across 26.5°N above 1000 m. We integrate the meridional geostrophic velocity between the African coast and three mooring sites 500, 40, and 16 km from Abaco, the Bahamas (mooring sites WB5, WB3, and WB2; see Figs. 1 and 2), between April 2004 and October 2006.

The RAPID–MOCHA system began monitoring daily variations in the strength and vertical structure of the AMOC in April 2004. To monitor midocean transport, the system consists of an array of moorings measuring salinity (S), temperature (T), and pressure (P) near the western boundary (mooring sites WB2, WBH1, WBH2, WB3, and WB5), the eastern boundary (EB1, EBHi, and EBH0–EBH5), and on both flanks of the Mid-Atlantic Ridge (MAR1 and MAR2; see Figs. 1–3). Vertical profiles of the densities at the western and eastern boundaries are used to compute estimates of the meridional geostrophic transport between the eastern boundary and the western boundary moorings (see Table 1). The western

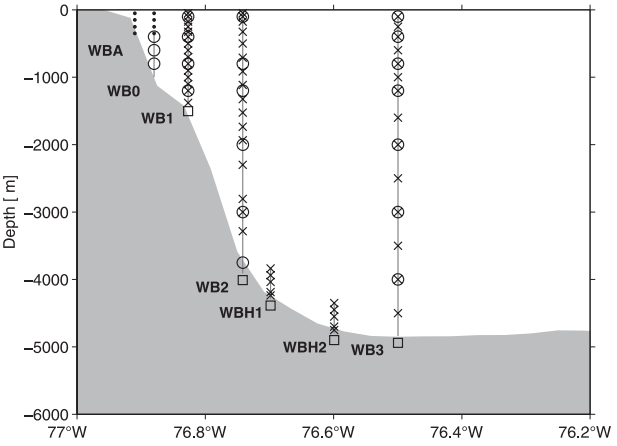

FIG. 3. Moorings near the western boundary (off Abaco, the Bahamas). Density sensors, bottom pressure recorders, and current meters are denoted as crosses, squares, and circles, respectively. The dots at WBA and WB0 indicate the part of the water column covered by ADCP measurements. WBH1 and WBH2 were only deployed during the period April 2004–April 2005.

TABLE 1. Instrument depths of MicroCAT CTDs and current meters on the different moorings at the western boundary during the different deployment periods.

Site	Period	CTD and its depth (m)	Current meter and its depth (m)
WBA	20 Mar–20 Oct 2004	N/A	ADCP covering top 400 m
WBA	10 May 2005–19 Mar 2006	N/A	ADCP covering top 590 m
WBA	19 Mar 2006–27 Mar 2007	N/A	ADCP covering top 590 m
WB01	26 Mar 2004–09 May 2005	N/A	387, 604, 804
WB02	10 May 2005–9 Oct 2006	N/A	423.6, 619.2, 826.6
WB11	27 Mar 2004–9 May 2005	N/A	66, 116, 258, 422, 551, 718, 912, 1103, 1355
WB12	10 May–21 Nov 2005	N/A	138, 258, 397, 482, 667, 852, 1046, 1241, 1392
WB13	23 Mar 2006–27 Mar 2007	50, 100, 175, 250, 325, 400, 500, 700, 900, 1000, 1100, 1200, 1380	100, 400, 800, 1200
WB21	26 Mar 2004–11 May 2005	98, 155, 303, 447, 654, 852, 1055, 1254, 1647, 2048, 2545, 3050, 3543, 3740	156, 438, 857, 1261, 2051, 3048, 3877
WB22	14 May 2005–20 Mar 2006	350, 550, 750, 950, 1150, 1560, 1915, 2500, 2980, 3470, 3820	1126, 1323, 1559, 1701, 2103, 2444, 2957, 3111, 3895
WB23	23 Mar–8 Oct 2006	50, 175, 325, 500, 700, 800, 900, 1100, 1300, 1500, 1700, 1900, 2250, 2750, 3250	100, 1200, 2000, 3000, 3750
WB24	11 Oct 2006–27 Mar 2007	50, 100, 175, 325, 500, 700, 900, 1100, 1300, 1500, 1700, 1900, 2250, 2750, 3250, 3750	100, 375, 800, 1200, 2086
WBH1	25 Mar 2004–9 May 2005	3821, 3926, 4033, 4192, 4237	N/A
WBH2	25 Mar 2004–9 May 2005	4304, 4407, 4511, 4679, 4728	N/A
WB31	24 Mar 2004–11 May 2005	50, 104, 250, 400, 600, 800, 1000, 1200, 1600, 2000, 2500, 3000, 4000	100, 400, 800, 1200, 2000, 3000, 4000
WB32	13 May 2005–6 Oct 2006	60, 100, 250, 400, 600, 800, 1000, 1200, 1600, 2000, 2500, 3000, 3500, 4000, 4500	100, 401, 811, 1210, 2019, 3025, 4031
WB51	21 Mar 2004–16 May 2005	50, 100, 400, 600, 800, 1000, 1200, 1600, 2000, 3000, 3500, 4000, 4500, 5000	50
WB52	17 May 2005–2 Oct 2006	50, 100, 250, 400, 600, 800, 1000, 1200, 1600, 2000, 2500, 3000, 3500, 4000, 4500, 5000	50

boundary end-of-section profile uses data merged from WB2 shallower than 4000 m and from WBH1–WBH2 (and WB3 after April 2005). Vertical profiles of S, T, and P have also been derived separately at WB3 and WB5. At the eastern boundary, S, T, and P data from all eastern boundary moorings have been merged into one profile from 4840 m to the shallowest available level during each deployment (Table 1; Kanzow et al. 2007).

Temperature, salinity, and pressure are sampled every 15 min and then 2-day low-pass filtered and subsampled ever 12 h (Kanzow et al. 2007; information available online at www.noc.soton.ac.uk/rapidmoc). Filtered and subsampled S, T, and P data at each site are vertically interpolated onto a 20-dbar grid (Kanzow et al. 2007) by applying an interpolation technique that makes use of climatological estimates of the vertical shape of the temperature and salinity profile [$dT/dP(T)$; $dS/dP(T)$] following Johns et al. (2005). Density is then computed from the 12-hourly S, T, and P profiles.

Moorings at sites WB0, WB1, WB2, and WB3 are instrumented with current meters (Fig. 3); in addition, at mooring sites WBA and WB0, acoustic Doppler current profilers (ADCPs) (Fig. 3) measure the velocity field in the upper 500 m (Johns et al. 2008). Velocity data are 40-h low-pass filtered and subsampled on a 12-hourly grid (Johns et al. 2008). At each time step velocities are interpolated onto a spatial grid with zonal and vertical resolutions of 500 and 20 m, respectively (Johns et al. 2008). The gridded velocity data are then used to compute profiles of zonally integrated transports per unit depth between the Abaco shelf and WB2 and between the Abaco shelf and WB3.

Bottom pressure (P_{BOT}) has been measured continuously throughout the 30 months at mooring sites WB3 and WB5. Combined with the density profiles from these two sites, we compute geostrophic transports between them. The P_{BOT} samples at 10-min intervals are 2-day low-pass filtered and subsequently subsampled on a 12-hourly basis (Kanzow et al. 2007). A long-term instrumental trend has been removed from each bottom pressure record by subtracting a least squares exponential-linear fit from the data of each deployment period (Watts and Kontoyiannis 1990). Finally, the time mean is removed (Fig. 4).

b. Methods

Meridional transports across 26.5°N zonally averaged between Florida and Africa and vertically averaged over the top 1000 m are a reliable measure of the strength of the Atlantic Meridional Overturning Circulation (Cunningham

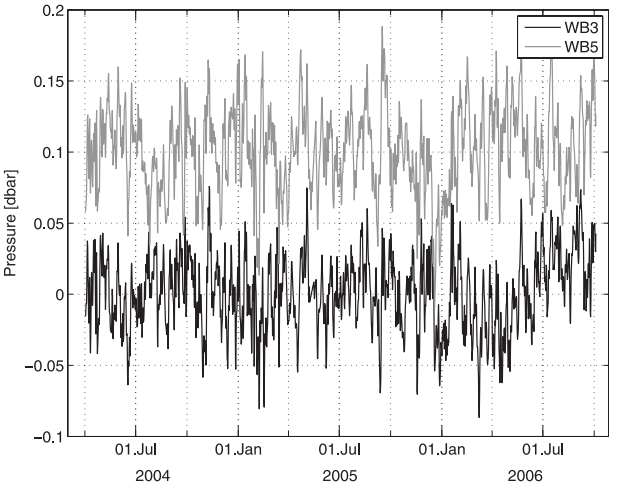

FIG. 4. The 48-h low-pass-filtered time series of bottom pressure fluctuations (time mean removed) at WB3 and WB5. An offset of 0.1 dbar has been added to the WB5 pressure record.

et al. 2007) because the middepth level of no motion exhibits fluctuations in vertical displacement of only 90 m RMS around its time mean of 1041 m for daily transport values. The basinwide integrated northward transport T_{BASIN} across 26.5°N is computed as the sum of (i) the zonally averaged Ekman transport T_{EK}, (ii) Gulf Stream transport integrated across the Straits of Florida (between Florida and the Bahamas) T_{GS}, and (iii) the midocean transport (the northward geostrophic transport integrated between the Bahamas and the African coast) T_{MO}:

$$T_{\mathrm{BASIN}}(z, t) = T_{\mathrm{GS}}(z, t) + T_{\mathrm{EK}}(z, t) + T_{\mathrm{MO}}(z, t). \quad (5)$$

The notation $T_{\mathrm{GS}}(z, t)$, $T_{\mathrm{EK}}(z, t)$, $T_{\mathrm{MO}}(z, t)$, etc., indicates transports per unit depth z, while $T_{\mathrm{GS}}(t)$, $T_{\mathrm{EK}}(t)$, $T_{\mathrm{MO}}(t)$, etc., indicate vertically integrated transports. As each variable is a function of time t, the explicit mentioning of the time dependence will be dropped hereafter. Transport fluctuations are anomalies about the time mean, unless otherwise noted.

For the computation of T_{EK}, we used daily wind stress data from the Quick Scatterometer (QuikSCAT) mission (Kanzow et al. 2007) while daily estimates of T_{GS} are available from the telephone cable–based Florida Current monitoring system (Baringer and Larsen 2001). The midocean transport $T_{\mathrm{MO}}(z, t)$ can be divided into two components: (i) the transport in the 16-km-wide "western boundary wedge" between the Abaco shelf (AS) and site WB2 $T_{\mathrm{AS\text{-}WB2}}(z)$, derived from direct current meter measurements on moorings WBA, WB0, WB1, and WB2 (Fig. 2; for details see Johns et al. 2008; Kanzow et al. 2008b) and (ii) the surface to 4740 m geostrophic transport between WB2 and the eastern boundary. The geostrophic transport relative to the reference level $z_{\mathrm{REF}} = -4740$ m between WB2 and the eastern boundary, referred to as *internal* transport T_{INT}, is computed from continuous observations of density profiles at the section endpoints (ρ_{WB2} and ρ_{EAST}) according to

$$T_{\mathrm{INT}}(z) = -\frac{g}{(f\rho)}\int_{Z_{\mathrm{REF}}}^{z} [\rho_{\mathrm{EAST}}(z') - \rho_{\mathrm{WB2}}(z')]\, dz. \quad (6)$$

To compute the absolute geostrophic transports, for each 12-hourly profile of $T_{\mathrm{INT}}(z)$, a reference transport T_C must be derived.

From the first year of the RAPID measurements, Kanzow et al. (2007) show that there is a strong negative correlation between T_{MO} and the sum of T_{GS} and T_{EK} at periods in excess of 10 days, such that the residual (zonally and vertically integrated) transport across 26.5°N displays much smaller fluctuations than either component. Kanzow et al. (2007) argue that the variability of the residual transport is mostly due to measurement uncertainties rather than real fluctuations that could have been caused by changes in the strength of the Arctic throughflow. Here, we assume that there is precise compensation among the different flow components, in the sense that the sea surface to seafloor ($z = -h_{\mathrm{BOT}}$) integral yields zero residual mass transport across 26.5°N (Kanzow et al. 2007; Cunningham et al. 2007) according to

$$\int_{-h_{\mathrm{BOT}}}^{0} [T_{\mathrm{GS}}(z) + T_{\mathrm{EK}}(z) + T_{\mathrm{MO}}(z)]\, dz = 0. \quad (7)$$

The *net upper midocean transport* U_{MO} is defined as the midocean transport $T_{\mathrm{MO}}(z)$ integrated over the upper 1000 m, according to

$$U_{\mathrm{MO}} = \int_{-1000}^{0} [T_{\mathrm{INT}}(z) + T_c(z) + T_{\mathrm{AS\text{-}WB2}}(z)]\, dz. \quad (8)$$

Formally, there is a small southward mass transport across 26.5°N associated with the sum of Bering Straits flow from the Pacific into the Arctic Ocean and of the net precipitation between the Bering Straits and 26.5°N. Because each of these components is less than 1 Sv and there is little information on how they vary in time (Woodgate and Aagaard 2005; Wijffels 2001), we assume zero residual mass transport at each moment of time and the referencing of $T_{\mathrm{INT}}(z)$ is carried out by computing a compensating transport profile T_C at each time step as follows:

$$T_C = -\int_{-h_{\mathrm{BOT}}}^{0} [T_{\mathrm{GS}}(z) + T_{\mathrm{EK}}(z) + T_{\mathrm{AS\text{-}WB2}}(z) + T_{\mathrm{INT}}(z)]\, dz. \quad (9)$$

For the computation of the corresponding compensation transport profile $T_C(z)$, we assume that the underlying compensating meridional velocity field V_C is spatially uniform (vertically and zonally) such that

$$T_C(z) = V_C \int_{X_W}^{X_E} dx = V_C L(z), \quad (10)$$

with X_E and X_W denoting the eastern and western boundaries, respectively, and L denoting the effective width of the ocean, which decreases with depth.

Throughout this study we apply a 10-day low-pass filter to U_{MO} (and to all other transport time series) as transport changes at periods shorter than 10 days may not be representative of AMOC fluctuations (Kanzow et al. 2007). As defined in (10) $T_C(z)$ is nearly depth independent shallower than 3500 m, whereas below that the reduction in the effective zonal ocean width (below the crest of the Mid-Atlantic Ridge; see Fig. 1) makes the amplitude of $T_C(z)$ decrease with depth. Overall, only about 25% of $T_C(z)$ occurs at depths shallower than 1000 m.

To compute the upper-ocean transport east of WB2 $U_{\mathrm{WB2\text{-}EAST}}$, we subtract from U_{MO} the transport west of WB2 in the upper 1000 m ($U_{\mathrm{AS\text{-}WB2}}$):

$$U_{\mathrm{WB2\text{-}EAST}} = U_{\mathrm{MO}} - \int_{-1000}^{0} T_{\mathrm{AS\text{-}WB2}}(z')\, dz. \quad (11)$$

Similarly, to obtain the upper midocean transport east of WB3 ($U_{\mathrm{WB3\text{-}EAST}}$), we subtract from U_{MO} the transport west of WB3 ($U_{\mathrm{AS\text{-}WB3}}$) integrated over the top 1000 m:

$$U_{\mathrm{WB3\text{-}EAST}} = U_{\mathrm{MO}} - \int_{-1000}^{0} T_{\mathrm{AS\text{-}WB3}}(z')\, dz. \quad (12)$$

Here, $U_{\mathrm{AS\text{-}WB3}}$ is computed from the direct current meter measurements on WBA, WB1, WB2, and WB3 (Fig. 3; Johns et al. 2008). Finally, to obtain the upper midocean transport east of WB5 ($U_{\mathrm{WB5\text{-}EAST}}$), we subtract from U_{MO} the sum of $U_{\mathrm{AS\text{-}WB3}}$ and the transport between WB3 and WB5 above 1000 m ($U_{\mathrm{WB3\text{-}WB5}}$):

$$U_{\mathrm{WB5\text{-}EAST}} = U_{\mathrm{MO}} - \int_{-1000}^{0} [T_{\mathrm{AS\text{-}WB3}}(z') + T_{\mathrm{WB3\text{-}WB5}}(z')]\, dz. \quad (13)$$

Here, $U_{\mathrm{WB3\text{-}WB5}}$ is computed in three steps. First, we compute the *internal* geostrophic transport relative to 4740 m between WB3 and WB5 from the density profiles at both sites (ρ_{WB3} and ρ_{WB5}) as in (6). Second, both mooring sites comprise bottom pressure sensors, from which the near-bottom northward *external* transport (per unit depth) $T_{\mathrm{EXT}}(z)$ integrated between WB3 and WB5 can be computed (e.g., Kanzow et al. 2008b) according to

$$T_{\mathrm{EXT}}(z) = \frac{1}{\rho f}[P_{\mathrm{WB5}}^{\mathrm{BOT}} - P_{\mathrm{WB3}}^{\mathrm{BOT}}]. \quad (14)$$

Finally, adding internal and external transports gives geostrophic transport fluctuations between WB3 and WB5 $T_{\mathrm{WB3\text{-}WB5}}(z)$.

We will compare the dynamic sea surface heights at the mooring locations and the midocean transport anomalies to satellite-derived sea surface heights and their zonal differences. We use the "updated" delayed-time maps of sea level anomalies (DT-MSLA "Upd") gridded multisatellite merged altimeter dataset described by Dibarboure et al. (2008) and provided by Aviso (information online at http://www.aviso.oceanobs.com). The altimetry dataset spans the period between October 1992 and January 2008 and has a nominal resolution of 1/3° in space and 7 days in time. The underlying satellite missions include TOPEX/Poseidon, *Jason-1*, *European Remote Sensing Satellite-2* (*ERS-2*), and *Envisat*. We extract the sea surface height η along 26.5°N and at each time step we subtract the zonal mean η (Bahamas to Morocco) from each grid point. This suppresses the dynamically inactive portion of the seasonal variations of η that is mainly associated with seasonal near–sea surface thermal expansion.

The *Jason-1* ground track closest to the Abaco shelf approaches to within about 4 km of WB2, crossing 26.5°N east of WB2. It is an ascending track that enters deep waters from the Nassau shelf about 200 km southwest of WB2 (Fig. 1b). The correlation between η at the point closest to WB2 from the *Jason-1* along-track dataset and η at WB2 extracted from the gridded dataset (with the latter being subject to spatial and temporal averaging) is $R = 0.79$. A descending *Jason-1* track approaches WB3 to within 15 km (minimum distance), crossing 26.5°N to the east of WB3 (Fig. 1b).

Throughout the paper anomalies of transport and sea surface height will be discussed such that T and η represent fluctuations with the time mean removed.

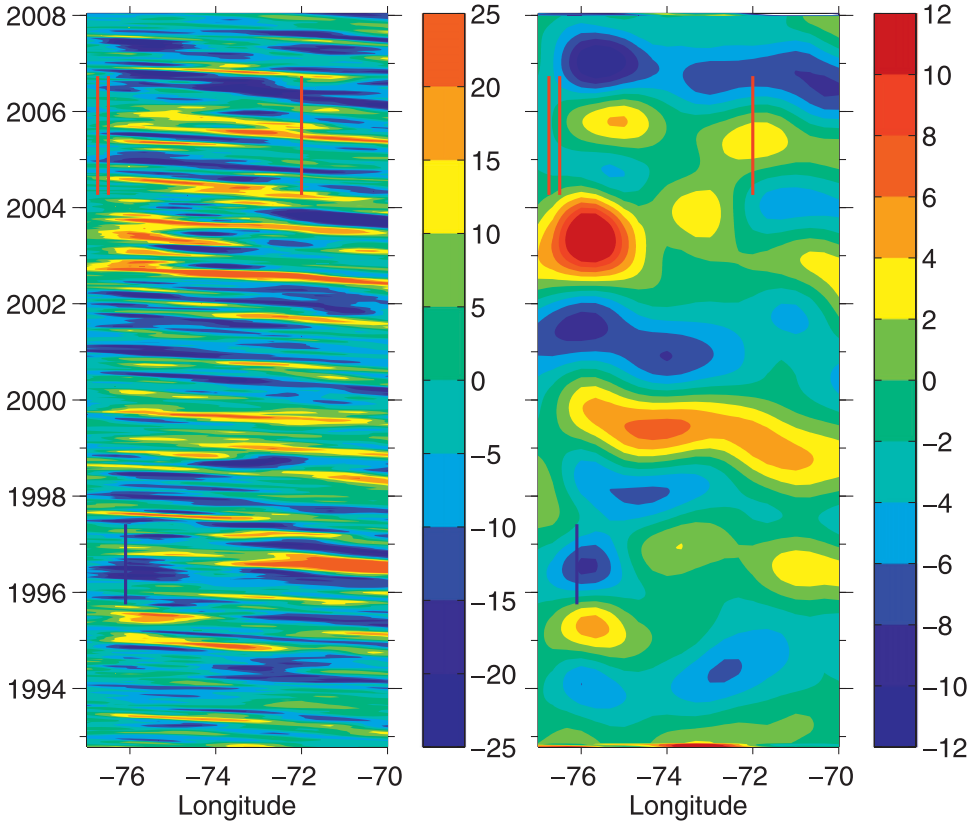

FIG. 5. (left) Sea surface height anomalies η (cm) along 26.5°N in the Atlantic from October 1992 to January 2008. The zonal mean (Bahamas to Morocco) has been subtracted at each time step. (right) Same as in the left panel but with a 730-day low-pass filter applied. The red lines in both panels indicate the April 2004–October 2006 interval during which mooring measurements at WB2, WB3, and WB5 were made. The blue line marks the interval of the density measurements made at mooring C from the ACCP-3 experiment (Johns et al. 2005) deployed at 26.5°N and 76.1°W between October 1995 and June 1997.

3. Upper-ocean transport and sea surface height

In the following, we test the extent to which altimetric observations of η can be used to gain information on the spatiotemporal characteristics of zonally integrated upper-ocean transport. Figure 5 shows η for the period between October 1992 and January 2008 within 700 km of the western boundary along 26.5°N. It reveals coherent westward propagation of η anomalies at roughly 6 cm s^{-1}, with periods between 2 and 6 months. However, some of the propagating anomalies entering the domain at 70°W disintegrate before they reach 76°W. For example, positive and negative anomalies appear at 70°W in June 1996 and July 2003 vanishing before crossing 74°W.

Superimposed on the propagation pattern are numerous isolated stationary anomalies that sometimes appear as dipolar structures. Three such events can be seen between 76° and 73°W during the period from October 2002 through July 2003. Interannual variations are also apparent, both propagating and stationary. The strongest interannual changes are centered around 75.8°W (Fig. 5b), where η displays anomalously negative values from February 2001 through June 2002 and from April 2006 through July 2007, and positive values from October 2002 through January 2004. Both stationary and propagating anomalies have in common that their RMS amplitudes and RMS variabilities appear to diminish west of 76°W.

In the western boundary region at 26.5°N, there is a gradual westward increase in the RMS fluctuations of η from 6.5 cm RMS at 65°W to its maximum 11.2 cm RMS at 75.8°W for the period of altimetric observations between October 1992 and January 2008 (solid line in Fig. 6). West of 75.8°W, there is a rapid decrease in the variability of η from 11.2 to 5.3 cm RMS at 76.75°W. Estimates of the RMS amplitude of η west of 76.75°W (WB2) are possibly unreliable due to a lack of altimetric observations. Similar reductions in RMS variability are confirmed for the shorter RAPID measurement period between April 2004 and October 2006 (red dashed line)

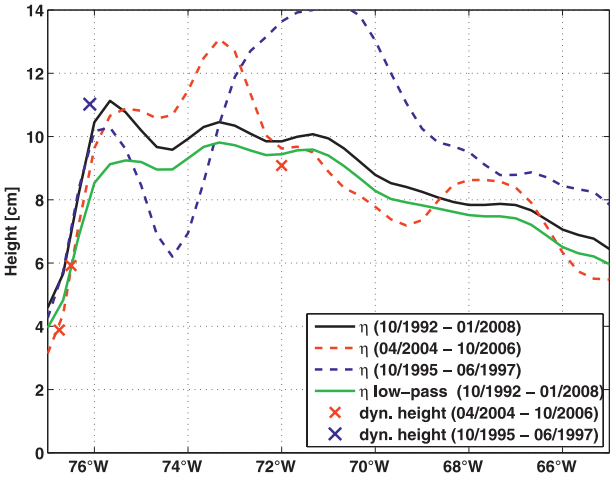

FIG. 6. RMS amplitude of η along 26.5°N for the intervals October 1992–January 2008 (solid black line), April 2004–October 2006 (red dashed line), and October 1995–June 1997 (blue dashed line). Also shown are the amplitudes of the RMS dynamic height fluctuations (dyn cm; i.e., geopotential anomaly divided by the earth's gravitational acceleration) at 200 m determined from the mooring density measurements at WB2, WB3, and WB5 (red crosses). The blue cross denotes the dynamic height computed from the density at mooring C of the ACCP-3 experiment (Johns et al. 2005). The green line shows the RMS amplitude of η along 26.5°N for 2-yr low-pass-filtered data for the interval October 1992–January 2008.

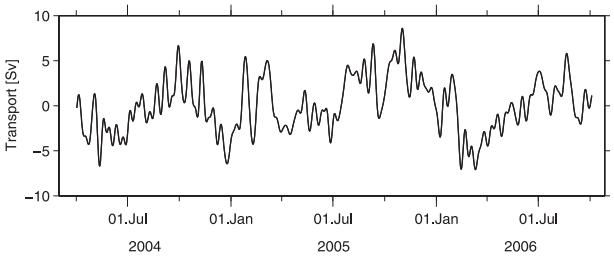

FIG. 7. Fluctuations of northward midocean transport above 1000 m (U_{MO}) between April 2004 and October 2006, 10-day low-pass filtered using a six-pole Butterworth filter.

and the Atlantic Climate Change Program (ACCP-3) measurement period (Johns et al. 2005) between October 1995 and June1997 (blue dashed line).

The rapid decrease of eddy energy toward the boundary may be due to the abrupt, clifflike topography of the Bahamian escarpment that deepens from 500- to 5000-m depth over 25 km. We show, however, that a decrease in eddy energy close to the western boundary is a general expectation from theory. This decrease in eddy energy within a few tens of kilometers of the western boundary differs from the general tendency for eddy energy to decrease away from energetic western boundary regions toward the ocean interior on scales of several hundred kilometers [as seen, e.g., in MODE-1 experiment a few degrees farther north (MODE-1 Atlas Group 1977)].

Also shown in Fig. 6 are RMS fluctuations of dynamic height at 200 m relative to the seafloor from the RAPID mooring measurements (red crosses) and from mooring C of the ACCP-3 experiment (Johns et al. 2005). Using a dynamic height at 200 m rather than at sea level suppresses the seasonal cycle of the near-surface thermal expansion. Dynamic heights at WB5, C, WB3, and WB2 vary by 9.1, 11.0, 5.9, and 3.9 dynamic cm RMS, respectively, and are in agreement with the altimetric observations (Fig. 6). In particular, the sharp decrease to the west of site C is reproduced. If RMS fluctuations of dynamic height from mooring C are representative of those during the RAPID measurement period, the implied decrease in dynamic height variations (or η) is 7.1 cm, declining from 11 cm at 76.1°W to 3.9 cm RMS at 76.75°W (i.e., over 65 km). This may be a steeper gradient than the gridded altimeter dataset can resolve with its resolution of about 33 km.

If η or the dynamic height near the sea surface can be used as a proxy for upper-ocean transport, then, according to (4), the meridional transport variations integrated between WB5 and the eastern boundary should be significantly larger than between WB2 and the eastern boundary. Note in passing that at the eastern boundary the RMS fluctuations of η amount to only 2.2 cm RMS at EBH4 (Fig. 2).

The 10-day low-pass-filtered basinwide integrated upper midocean transport U_{MO} exhibits fluctuations of 3.0 Sv RMS over the 30 months of observations (Fig. 7; Table 2). It shows pronounced seasonal variations that suggest a reduced southward flow in autumn and enhanced southward flow in spring. The standard error of U_{MO} (based on the degrees of freedom in Table 2) is 0.6 Sv for the 30-month-long time series and 0.9 Sv for a 12-month segment.

The upper-ocean transport between WB2 and the eastern boundary ($U_{WB2\text{-}EAST}$) displays a variability of 3.6 Sv RMS and a correlation of 0.81 with U_{MO}, which is significant at 5% error probability (Table 2; Fig. 8). Transports between WB3 and the eastern boundary ($U_{WB3\text{-}EAST}$) and between WB5 and the eastern boundary ($U_{WB5\text{-}EAST}$) exhibit variations of 6.0 and 10.8 Sv RMS, respectively (Table 2; Fig. 8). The correlations of $U_{WB3\text{-}EAST}$ and $U_{WB5\text{-}EAST}$ with U_{MO} are 0.45 and 0.10, respectively, with the first value being barely significant and the second not exceeding the 5% error probability threshold of 0.42 (Table 2). The differences $U_{WB2\text{-}EAST} - U_{MO}$ and $U_{WB3\text{-}EAST} - U_{MO}$ are 2.1 and 5.3 Sv RMS, respectively.

The following picture emerges within roughly 100 km of the western boundary of the Atlantic at 26.5°N. The

TABLE 2. Transport statistics for upper-ocean transport (shallower than 1000 m). Columns 2–4 show transport standard deviations (the values in parentheses correspond to the 60-day low-pass- and high-pass-filtered time series), degrees of freedom for the 30-month records, and correlations of the transport to upper midocean transport U_{MO}, respectively. Column 5 indicates the correlation of transports with η at the mooring locations. Column 6 shows the RMS transport error if η is used to predict transport, assuming a linear relation $U_{WBX\text{-}EAST} = s_{WBX}(\eta_{EAST} - \eta_{WBX})$. Column 7 gives the transport variance (Sv) explained by η based on the aforementioned linear relationship. Calculations are based on 10-day low-pass-filtered data. The integral time scales underlying the degrees of freedom in column 3 represent the integrals of the autocorrelation function to the first zero crossing.

Variable	Transport std dev (Sv)	DOF	Correlation to U_{MO}	Correlation to $\eta_{EAST} - \eta_{WBX}$	RMS error using $\eta_{EAST} - \eta_{WBX}$ (Sv)	Variance explained by $\eta_{EAST} - \eta_{WBX}$ (%)
U_{MO}	3.0 (2.5/1.7)	22	1	0.12/WB1	—	No skill
$U_{WB2\text{-}EAST}$	3.6 (3.2/1.7)	23	0.81	0.44/WB2	3.2	19
$U_{WB3\text{-}EAST}$	6.0 (5.6/2.1)	23	0.45	0.71/WB3	4.2	51
$U_{WB5\text{-}EAST}$	10.8 (10.2/3.0)	15	0.10	0.85/WB5	5.7	72

farther away from the Abaco shelf the western endpoint of the section is moved to the east, the larger the variations of the zonally integrated transports become. We see that $U_{WB2\text{-}EAST}$, $U_{WB3\text{-}EAST}$, and $U_{WB5\text{-}EAST}$ exceed U_{MO} by factors of 1.2, 2, and 3.6, respectively, in terms of RMS fluctuations. The increase in transport variations is in qualitative agreement with the offshore increase in the RMS amplitude of η in the vicinity of the western boundary. This holds both for intraseasonal and interannual fluctuations (Fig. 6). The correlation analysis suggests that $U_{WB2\text{-}EAST}$ is moderately representative of U_{MO} with an RMS uncertainty of 2.1 Sv (which is not small compared to the 3.0 Sv RMS fluctuations of U_{MO}). The 2.1 Sv RMS is, according to (8), the RMS variability that the upper-ocean transports west of WB2 ($U_{AS\text{-}WB2}$) contributes. A negative correlation of −0.55 between $U_{WB2\text{-}EAST}$ and $U_{AS\text{-}WB2}$ is observed—possibly resulting from Antilles Current meanders and eddies passing over WB2—and explains why $U_{WB2\text{-}EAST}$ displays a larger transport fluctuations than does U_{MO}.

The transport components farther offshore (i.e., $U_{WB3\text{-}EAST}$, $U_{WB5\text{-}EAST}$) cannot serve as a reliable measure of U_{MO}. Thus, to estimate variations in U_{MO} reliably (as part of the AMOC at 26.5°N), density measurements have to be obtained as close to the boundary as possible (and not several tens of kilometers away from it).

We now test whether zonal differences in η provide a straightforward way of estimating zonally integrated upper-ocean transports across 26.5°N. The correlations of the differences in η between the eastern boundary and WB5, WB3, WB2, and WB1 ($\eta_{EAST} - \eta_{WBX}$, with X = 5, 3, 2, and 1 denoting the different WB mooring sites) with the corresponding transports $U_{WB5\text{-}EAST}$, $U_{WB3\text{-}EAST}$, $U_{WB2\text{-}EAST}$, and U_{MO} are 0.85, 0.71, 0.44, and 0.12, respectively (Fig. 9). The difference $\eta_{EAST} - \eta_{WB1}$ was used to compare to U_{MO} rather than η at the Abaco shelf break, because (i) variations of $U_{WB1\text{-}EAST}$ (i.e., upper-ocean transport east of WB1) are representative of U_{MO} with their correlation being 0.95 and (ii) sea surface variations from the gridded altimetry dataset to the west of WB2 are unreliable due to a lack of measurements (section 2). A linear regression of the form $U_{WBX\text{-}EAST} = s_{WBX}(\eta_{EAST} - \eta_{WBX})$ gives s_{WBX} = 0.91, 0.68, and 0.32 Sv cm^{-1} for $U_{WB5\text{-}EAST}$, $U_{WB3\text{-}EAST}$, and $U_{WB2\text{-}EAST}$, respectively. Subtracting the fit from the respective upper-ocean transports yields transport residuals $U_{WBX\text{-}EAST} - s_{WBX}(\eta_{EAST} - \eta_{WBX})$ of 5.7, 4.2, and 3.2 Sv RMS for X = 5, 3, and 2.

The linear fit using $\eta_{EAST} - \eta_{WBX}$ explains 72%, 51%, and 19% of the variances of $U_{WB5\text{-}EAST}$, $U_{WB3\text{-}EAST}$, and $U_{WB2\text{-}EAST}$, respectively. Although the transport variance explained by $\eta_{EAST} - \eta_{WBX}$ is largest at WB5, the absolute residual between the linear fit and the corresponding transport is largest, too. Both the relative

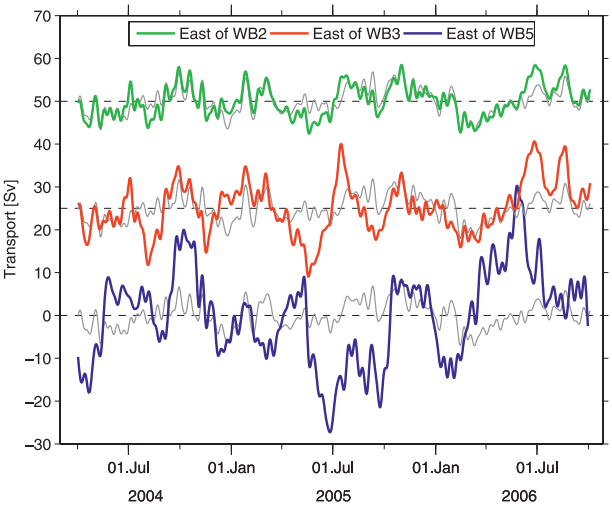

FIG. 8. Northward transport fluctuation (Sv) above 1000 m east of WB2 ($U_{WB2\text{-}EAST}$, green), east of WB3 ($U_{WB3\text{-}EAST}$, red), and east of WB5 ($U_{WB5\text{-}EAST}$, blue). For better visualization the transports are offset by 25 Sv (dashed lines represent the zero lines). Each of the three gray lines represents fluctuations of the upper midocean transport (to which the same offset has been applied to facilitate comparisons to the colored time series).

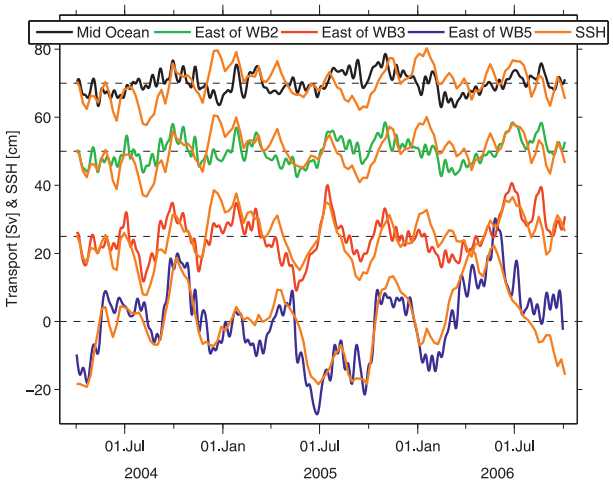

FIG. 9. Transports (Sv) of U_{MO} (black), $U_{WB2\text{-}EAST}$ (green), $U_{WB3\text{-}EAST}$ (red), and $U_{WB5\text{-}EAST}$. Superimposed (orange) are fluctuations of the difference in sea surface height (cm) between the eastern boundary (27°54.5′N, 13°22.0′W) and the locations of WB1, WB2, WB3, and WB5 extracted from the gridded altimeter dataset ($\eta_{EAST} - \eta_{WBX}$ with $X = 5, 3, 2$, and 1 denoting the different WB mooring sites). The difference $\eta_{EAST} - \eta_{WB1}$ was used to compare to U_{MO} rather than η at the Abaco shelf break (see text).

prediction skill and the absolute error decrease toward the boundary. At WB2, the error of the transport prediction (3.2 Sv RMS) has roughly the same amplitude as U_{MO}. This means that reliable estimates of U_{MO} cannot be obtained by combining a current meter–based boundary current array (measuring the transports between the shelf and, say, WB2) with altimetric observations of $\eta_{EAST} - \eta_{WB2}$.

The fact that $\eta_{EAST} - \eta_{WB1}$ has no skill in determining U_{MO} could partly be related to the fact that the *Jason-1* altimeter (or TOPEX/Poseidon) takes no measurements between Abaco and WB2. However, since there is a *Jason-1* ground track 4 km east of WB2, we consider the relatively low level of the variance of $U_{WB2\text{-}EAST}$ explained by $\eta_{EAST} - \eta_{WB2}$ to be a robust result.

It is interesting to note that it is particularly the low-frequency transport variability of periods in excess of 2 months that is gradually suppressed, as the western endpoint of the section is moved closer to the western boundary. The reduction in RMS transport variability is a factor of 4 comparing 2-month low-pass-filtered time series of $U_{WB5\text{-}EAST}$ and U_{MO} from 10.2 to 2.5 Sv RMS (Table 2). For 2-month high-pass-filtered data, there is only a reduction by a factor of 2 between $U_{WB5\text{-}EAST}$ and U_{MO} from 3.0 to 1.7 Sv RMS (Table 2). This will become relevant in section 6.

To investigate why the correlation between $U_{WB2\text{-}EAST}$ and $\eta_{EAST} - \eta_{WB2}$ is lower than the correlation between $U_{WB5\text{-}EAST}$ and $\eta_{EAST} - \eta_{WB5}$, an EOF mode analysis is carried out. The first three leading EOF modes for $U_{MO}(z)$, $U_{WB2\text{-}EAST}(z)$, $U_{WB3\text{-}EAST}(z)$, and $U_{WB5\text{-}EAST}(z)$ [which are the transport per unit depth profiles in the upper 1000 m corresponding to the net upper-ocean transports defined in (8) and (11)–(13)] are displayed in Figs. 10a–d. The variances explained by the first modes are 69%, 76%, 83%, and 92%, respectively, while those of the second modes amount to 22%, 18%, 17%, and 7%.

For all four transport cases the first modes (blue lines in Figs. 10a–d) do not exhibit a zero crossing between the sea surface and 1000 m. Therefore, the transport at the sea surface associated with the first mode is of the same sign as the upper-ocean transport explained by the first mode (i.e., the vertical integral of that mode over the top 1000 m). All of the second modes (red lines in Figs. 10a–d) display a zero crossing shallower than 250 m. As a result, transports associated with the second modes at the sea surface have opposite signs to the vertically integrated transports. The first modes of $U_{WB5\text{-}EAST}(z)$, $U_{WB3\text{-}EAST}(z)$, $U_{WB2\text{-}EAST}(z)$, and $U_{MO}(z)$ explain 10.8, 5.9, 3.5, and 2.8 Sv RMS above 1000 m, respectively, according to $\langle U^i_{WBX\text{-}EAST}\rangle^{1/2} = \langle A^i_{WBX\text{-}EAST}\rangle^{1/2} \int_{-1000}^{0} M^i_{WBX\text{-}EAST}(z)\,dz$, while the second modes account for 0.8, 0.9, 1.0, and 1.2 Sv RMS, respectively. Here, M^i denotes the ith EOF mode and A^i the corresponding principal component, and the angle brackets represent variance operators.

The gradient in the sea surface height is regarded as a measure of the surface geostrophic flow. For the former to be also a good indicator of depth-integrated upper-ocean transport requires surface and upper-ocean transport to fluctuate in phase. It is not surprising that $\eta_{EAST} - \eta_{WB5}$ is a good proxy of $U_{WB5\text{-}EAST}$ (Fig. 9) given that the first EOF mode explains 92% of the variance (Fig. 10d). Flow reversals in the upper 1000 m—as represented by the second EOF modes—gradually gain in importance as the western endpoint of the transport integration is moved westward. As has been shown above, all of the second modes imply an out-of-phase relationship between the surface and the depth-integrated upper-ocean transport. In the particular case of the Bahamaian western boundary, this has to do with the superposition of the upper-ocean Antilles Current on the DWBC below, which have been shown to vary largely independently from one another (Lee et al. 1990, 1996). Further, the core of the Antilles Current, which is found near 400 m in the mean, is not strongly coupled to variations in the surface currents just above it (Lee et al. 1990, 1996).

The change of the modal structure over the continental slope implies that the clear relationship between the surface and the upper-ocean transport found offshore is gradually lost. As a consequence, variations in $\eta_{EAST} - \eta_{WB2}$ do not provide a reliable estimate of the

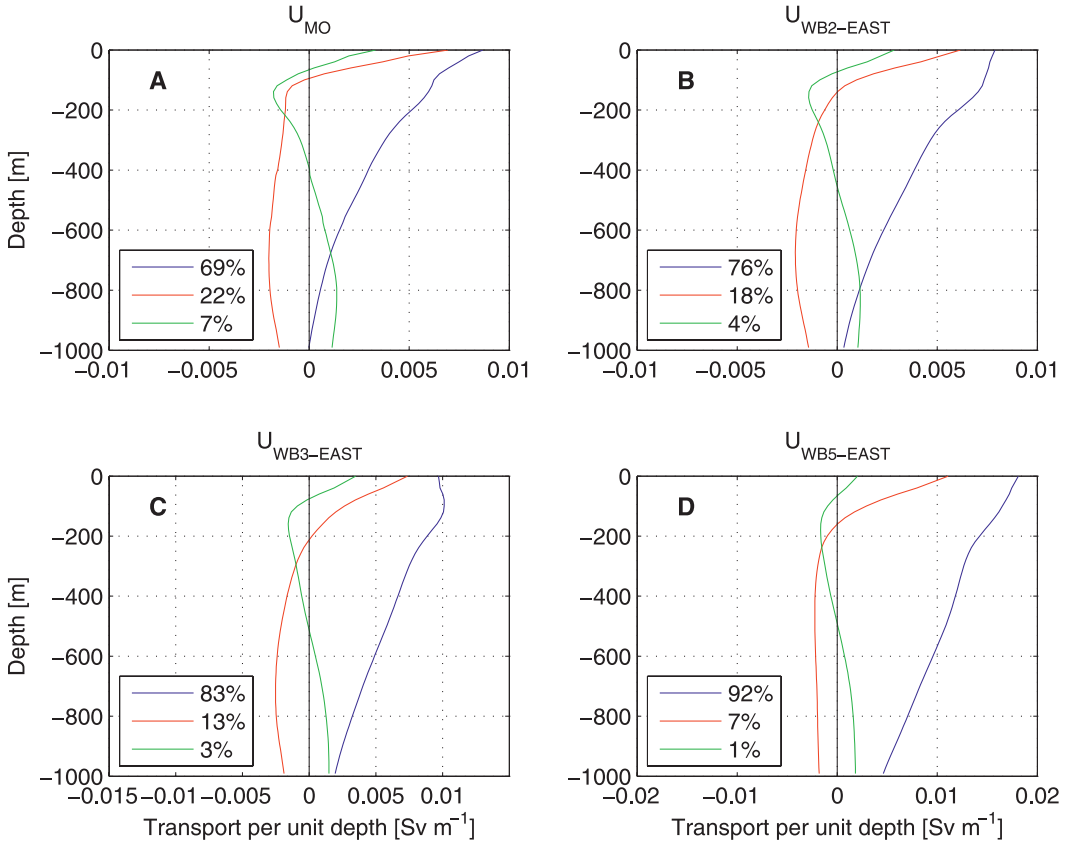

FIG. 10. First three EOF modes for 10-day low-pass-filtered transport per unit depth profiles of (a) U_{MO}, (b) $U_{WB2\text{-}EAST}$, (c) $U_{WB3\text{-}EAST}$, and (d) $U_{WB5\text{-}EAST}$. The time-averaged transport profile has been removed prior to the computation of the modes. The modes exhibit units of Sv m^{-1}, since they have been multiplied by the standard deviation of the corresponding principal components. This way the amplitudes of the different modes can be compared at each depth level. The legends indicate the variances explained by each mode.

temporal evolution of $U_{WB2\text{-}EAST}$ (Fig. 9). In the case of U_{MO}, the second mode has an even higher relative importance than the first one, when compared to $U_{WB2\text{-}EAST}$ (Figs. 10a and 10b). The fact that altimetric measurements effectively do not exist west of WB2 represents an additional practical problem when trying to infer the temporal evolution of U_{MO} (as part the AMOC) from the basinwide gradient of the sea surface height.

4. The signatures of eddies in basinwide integrated transports: A model simulation

Why are upper-ocean transport variations integrated between the western and eastern boundaries so much smaller than WB5-to-eastern boundary transports? And what is the dynamical reason for the sharp decline in RMS variations of the sea surface height anomalies within 100 km of the western boundary? Analysis of the altimeter data suggests that westward-propagating eddies are a major source of variability near the western boundary (Fig. 5). In this section we present numerical results from a nonlinear reduced-gravity model. We want to elucidate the fate of Rossby waves and eddies as they approach the western boundary and to investigate how they affect the sea surface height near and on the boundary. This allows us to put the observations into a dynamical context.

The model is similar to that described in Johnson and Marshall (2002) but is eddy permitting with a lateral resolution of 14 km. The domain extends 4500 km in the meridional direction (with the southern boundary at the equator) and 2800 km in the zonal direction. A beta-plane approximation is made, with $f_0 = 0.65 \times 10^{-4}$ s $^{-1}$ equal to the Coriolis parameter at 26.5°N. The background model layer thickness is 750 m, and the reduced gravity is 0.015 m s^{-2} (broadly consistent with the North Atlantic density distribution). Dissipation is achieved through lateral friction, with a coefficient of 30 m^2 s^{-1}, and no-slip and no-normal flow boundary conditions are applied. A sponge region ramps up over the southernmost

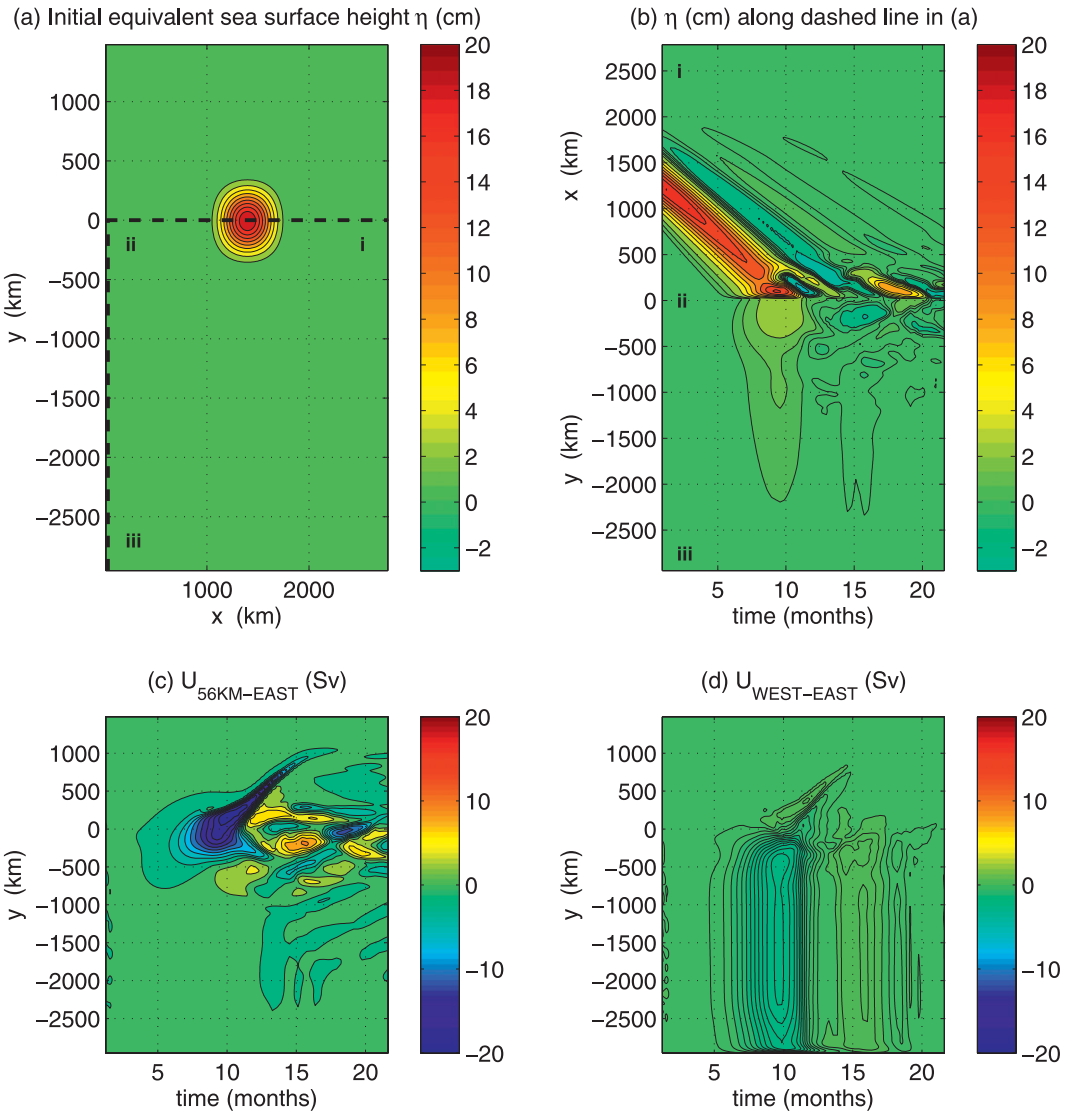

FIG. 11. Results of a numerical calculation with a reduced-gravity model, initialized with a single anticyclonic eddy of 500 km in diameter at $y = 0$ (equivalent to 26.5°N) and 1400 km from the western boundary. (a) The initial sea surface height η in cm (contour interval 2 cm). (b) A Hovmöller diagram of η along the dashed line in (a) along $y = 0$ and then down the western boundary (contours at ±0.5, ±1, and ±2 and then every 2 cm). (c) A Hovmöller plot of net northward transport within the upper model layer, integrated zonally from 56 km away from the western boundary to the eastern boundary, as a function of latitude and time (contour interval is 2 Sv). (d) The net northward transport integrated from coast to coast, again as a function of latitude and time; the color scale is the same as in (c) and the contour interval is 0.2 Sv.

1000 km of the domain, in which layer thickness is relaxed to the background value at a maximum rate of $\frac{1}{6}$ h^{-1}; this efficiently damps any fast boundary waves as they approach the equator, preventing them from propagating right around the basin and contaminating the results.

The first integration (Fig. 11) is initialized with a single, anticyclonic eddy, located roughly in the center of the domain at $y = 0$ (equivalent to 26.5°N). The eddy has an approximate diameter of 500 km, and a layer thickness anomaly of 130 m, equivalent to a sea surface height anomaly, $\eta' = (g'/g)h'$, of roughly 20 cm, as plotted in Fig. 11a. The eddy propagates westward at a speed of about 5 cm s^{-1} (Fig. 11b) although it is somewhat dispersive. On reaching the western boundary, a fast Kelvin wave is generated, which propagates rapidly southward; subsequently, the eddy itself propagates northward along the boundary due to the nonlinear image effect (Minato

1982) and the rocket effect (Nof 1988), and short Rossby waves are also generated. The maximum amplitude of the free-surface height disturbance η on the boundary is roughly a factor of 4 smaller than that in the basin interior.

Figures 11c and 11d show integrated meridional transports within the moving layer of the reduced gravity model, as a function of latitude and time. In Fig. 11c, the transport is integrated from 56 km off the western boundary to the eastern boundary ($U_{56\text{KM-EAST}}$); Fig. 11d shows the meridional transport integrated from coast to coast, from the western to the eastern boundaries ($U_{\text{WEST-EAST}}$). These two transport values differ widely in terms of both their structures and their amplitudes. While $U_{56\text{KM-EAST}}$ is dominated by the signature of the northward-moving eddy close to the western boundary, $U_{\text{WEST-EAST}}$ is dominated instead by the much smaller-amplitude, southward-propagating boundary wave signals on the western boundary itself. It is clear from Figs. 11c and 11d that the net northward transport anomaly associated with an individual eddy is very different when the western endpoint of the section lies a short distance off the boundary compared with on the boundary. This is a direct consequence of the reduction in amplitude of variations in η at the boundary.

Figure 12 shows the same diagnostics for a calculation in which the model is initialized with a field of cyclonic and anticyclonic eddies (Fig. 12a). The Hovmöller plot shows the westward propagation of the eddies along $y = 0$ and subsequent propagation along the western boundary (Fig. 12b); again, the maximum amplitude of η on the boundary is smaller than that in the basin interior. This is consistent with the observed reduction in the amplitude of the dynamic height variability between site C and WB2 (Fig. 6). As with the single eddy, $U_{56\text{KM-EAST}}$ exhibits large-amplitude variability (Fig. 12c), most of which disappears in $U_{\text{WEST-EAST}}$ (Fig. 12d), and the remaining transport anomaly being associated with boundary waves generated when each eddy reaches the western boundary. Figure 13a shows variations of η along 26.5°N within 500 km from the western boundary (blow-up of image detail in Fig. 12b). As in the observation (Fig. 5), the simulated η anomalies display maximum amplitudes away from the western boundary. The RMS variability of η peaks at 100 km offshore (Fig. 13b) and there is then a decay of roughly a factor of 5 toward the western boundary. Both the scale over which the decay takes place and the degree of the decay are in good agreement with the observations (Fig. 6).

Note that the 1.5-layer reduced-gravity model used here includes no representation of topographic effects or boundary complexity, and as such does not accurately reproduce the details of the boundary propagation, which in more complex models involves a combination of Kelvin, mixed Kelvin–Rossby, and topographic Rossby wave dynamics (Huthnance 1978; Clarke and Shi 1991; Hallberg and Rhines 1996). However, we believe that the fact that the model exhibits a similar decay in the amplitude of variability as that observed, and over a similar distance from the boundary, suggests that these details are not necessary to explain the observed behavior. O'Rourke (2009) finds that the presence of topography in fact increases the speed of coastally trapped waves, provided that there are boundary waves with a group speed significantly faster than the interior Rossby wave speed, then a reduction in the amplitude of variability close to the boundary will occur.

The "eddy-filled ocean" experiment in Fig. 12 also highlights a potential attribution problem. The fast equatorward communication of transport anomalies may make it very difficult to distinguish between local and remotely forced fluctuations of U_{MO} (or the AMOC) because—at any given latitude—in addition to local anomalies U_{MO} also contains transport contributions resulting from eddies impinging on the western boundary poleward of the latitude of interest.

5. A theory for the reduction of SSH fluctuations close to the western boundary

The observations are in good qualitative agreement with the reduced-gravity model. In addition the model has highlighted boundary waves as a potential mechanism for reducing variability in η at the boundary. On the basis of linear dynamics, we now derive a relationship between the amplitude of η (or layer thickness anomaly) on the western boundary and the amplitude offshore.

First, consider an analytical model of linear Rossby waves in a β-plane basin. In the limit $\omega \ll \beta L_d$, the reduced-gravity equations admit long and short Rossby wave solutions,[2] satisfying the dispersion relations $\omega/k_l = -\beta L_d^2$ (for long waves) and $\omega k_s = -\beta$ (for short waves), where ω is the angular frequency, k_l and k_s are the long and short wavenumbers, L_d is the deformation radius, and β is the meridional gradient of f.

Now suppose that incoming long Rossby waves are balanced by short Rossby waves generated at a meridional western boundary ($x = 0$). The total layer thickness anomaly is thus

$$h' = A_l(y)e^{i(k_l x-\omega t)} + A_s(y)e^{i(k_s x-\omega t)}. \qquad (15)$$

[2] Clarke and Shi (1991) discuss this scaling. The distinction between long and short waves only works if this condition is met. Waves with higher frequencies become trapped at the boundary as Kelvin waves.

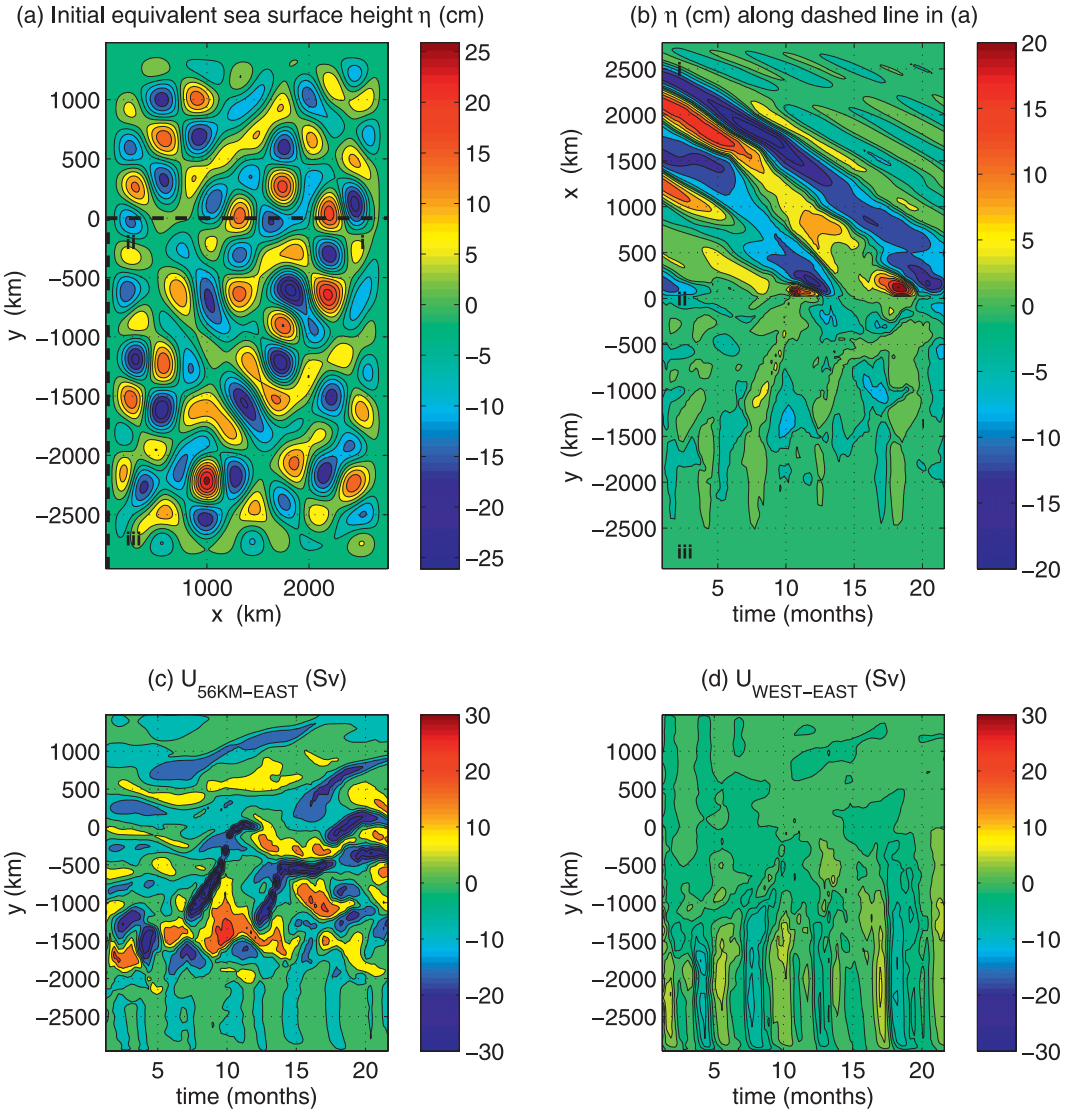

FIG. 12. As in Fig. 11, but for an integration initialized with a field of cyclonic and anticyclonic eddies. Contour intervals are (a) 4 cm; (b) ±1, ±4, and then every 4 cm; (c) 8 Sv; and (d) 2 Sv.

The wave amplitudes, $A_l(y)$ and $A_s(y)$, may be complex and include phase information.

The zonal component of velocity is zero at the western boundary. Thus, the linear meridional momentum equation [e.g., see Cushman-Roisin 1994, Eqs. (12)–(35), for the nonlinear case] takes the following form on the boundary:

$$\frac{\partial}{\partial t}\left(\frac{g'}{f}\frac{\partial h'}{\partial x}\right) + g'\frac{\partial h'}{\partial y} = 0. \tag{16}$$

Here, g' is the reduced gravity, we assume that the meridional velocity is geostrophic to leading order, and we neglect any frictional dissipation. Substituting for h', and noting $k_s \gg k_l$, we find

$$-\frac{\beta A_s}{f} + \frac{d}{dy}(A_l + A_s) \approx 0. \tag{17}$$

This, in turn, may be rewritten as

$$\frac{d}{dy}\left(\frac{A_l + A_s}{f}\right) \approx -\frac{\beta A_l}{f^2}. \tag{18}$$

Finally, assuming that the total wave amplitude, $A_s + A_l$, vanishes to the north of the incoming long waves, and integrating the above expression, we obtain

$$A_l + A_s \approx f\int \frac{\beta A_l}{f^2}\, dy \sim \frac{\beta \Delta y}{f}|A_l|. \tag{19}$$

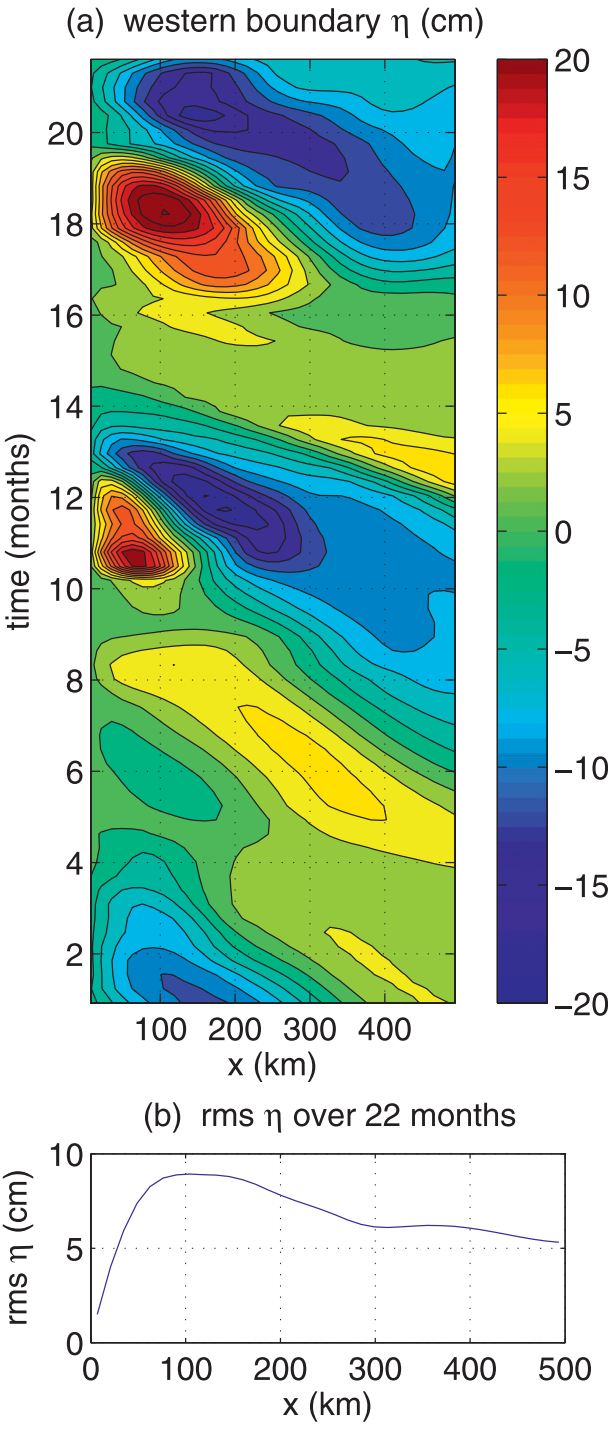

FIG. 13. (a) Hovmöller diagram of η along 26.5°N within 500 km of the western boundary and (b) RMS fluctuations of η from (a) as a function of distance from the western boundary.

Thus, the total wave amplitude on the boundary, $A_s + A_I$, is reduced relative to the interior by a factor $\beta\Delta y/f$, equal to the fractional change in the Coriolis parameter across the band of incoming long waves. The amplitude reduction is thus greater the smaller the meridional scale of the incoming wave (or eddy). If the incoming waves are confined to a small latitude band, then the wave amplitude, and hence the variability in sea surface height, are greatly reduced on the boundary. For $\Delta y = 500$ km, the reduction will be by a factor of $f/(\beta\Delta y) = 6$ (using $f_{26.5°N} = 6.4 \times 10^{-5}$ s^{-1} and $\beta = 2.1 \times 10^{-11}$ s^{-1} m^{-1}).

Physically, this amplitude reduction occurs because an along-boundary pressure gradient is unable to be maintained, since the Coriolis force to balance it would require a flow into the boundary. Instead a fluid acceleration is generated, which rapidly propagates any pressure anomalies along the boundary. This is precisely the same mechanism that gives rise to coastal Kelvin waves, although the character of the wave motion is different in this Rossby wave limit (Clarke and Shi 1991). The result that the pressure anomaly is reduced on the boundary holds across a wide range of physical parameters, although precise details depend on frictional dissipation, boundary conditions, and wave frequency (D. P. Marshall and H. L. Johnson 2009, unpublished manuscript).

6. Discussion

a. *Estimating the western boundary eddy contribution to upper midocean transports from altimetry*

Wunsch (2008) attempted to estimate the RMS variability of U_{MO} by projecting variations in η onto dynamical vertical modes of horizontal velocities. He argued that η near the western boundary of the subtropical Atlantic displayed typical variations of 16 cm RMS while exceeding those at the eastern boundary by a factor of 4.

Upon making assumptions about the spectral properties of η, he simulated an 80-yr-long time series of monthly values of U_{MO} (excluding Gulf Stream and Ekman transports), which exhibited fluctuations of 16 Sv RMS, distributed over a broad range from intraseasonal to decadal time scales. According to Wunsch (2008), the variations in U_{MO} were due to eddy variability with a decorrelation scale of not more than several tens of kilometers. He argued that the high degree of eddy variability in his simulation had the potential to mask possible climate change–related trends in the strength of the AMOC (Schmittner et al. 2005) for more than a century.

Our results imply that variability in η of 16 cm RMS may be regarded as typical of conditions found at 26.5°N between 100 and 500 km away from the western boundary, but not of conditions over the steep continental slope. Both altimetry and our measurements of dynamic height

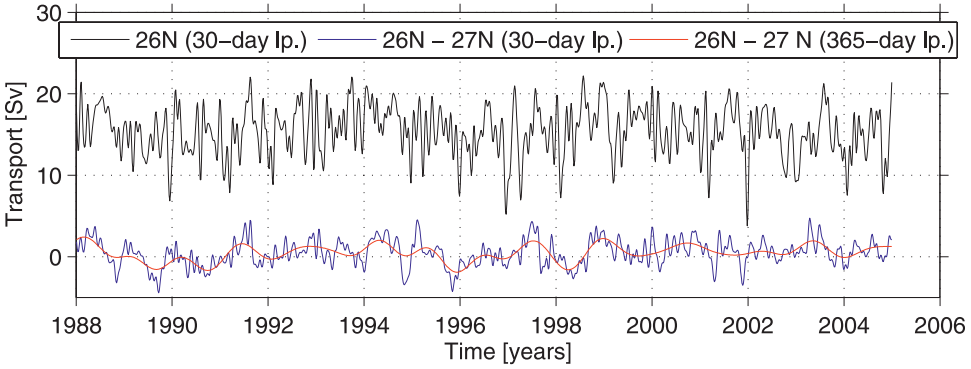

FIG. 14. Strength of the AMOC at 26°N from 1988 through 2004, defined as maximum upper-ocean northward transport in the OCCAM 1/12° model for 30-day low-pass-filtered values (black line). The blue and red lines represent the differences in AMOC strength between 26° and 27°N for 30-day and 365-day low-pass-filtered values.

suggest that an RMS value between 3 and 5 cm is appropriate. Wunsch assumes that the amplitude of η of 16 cm RMS is linked to the amplitude of U_{MO}, which readily explains why his estimate of the amplitude of U_{MO} of 16 Sv RMS is too large by a factor of 3–5, when compared to the 3.0 Sv RMS we have observed. The actual impacts of eddy variability on the observed intraseasonal and seasonal variability of U_{MO} are much smaller than implied by Wunsch's interpretation.

We have shown from in situ observations, altimetry, and numerical modeling that there is a rapid westward decrease in the variability of η within 100 km of the Abaco shelf. Boundary waves play an important role in explaining this decline, as they provide a fast mechanism for the along-boundary export of transport anomalies originating from eddies and Rossby waves impinging on the western boundary. The statistical approach of Wunsch (2008) does not include western boundary dynamics and therefore cannot account for the decline.

Wunsch (2008) argues that an observed time series of U_{MO} of only 12-month length (Cunningham et al. 2007) may display significantly less variability than the same time series spanning years or decades. Over the RAPID observational period (April 2004–January 2006), the variability of η amounts to 3.8 cm RMS at mooring site WB2, corresponding to U_{MO} variations of 3.0 Sv RMS. The 15-yr-long time series of η (from January 1992 to January 2008) has an RMS variability of 5.3 cm. We estimate that U_{MO} spanning one or two decades could display fluctuations of 3 Sv (5.3 cm/3.8 cm) = 4.2 Sv. We therefore expect the actual influence of eddy variability on a decade-long time series of U_{MO} to be 4 times less than suggested by Wunsch—and possibly smaller—since not all the contributions to the variability in U_{MO} stem from eddy-generated density variations at the western boundary.

The standard error of the mean gives an indication of changes in U_{MO} that can be resolved over any interval (SE = $\sigma/\sqrt{\text{DOF}}$, where σ is the standard deviation and DOF is the number of degrees of freedom). For the 30-month record (Table 2), we estimate that there are 22 degrees of freedom or, effectively, nine independent measurements per year. Assuming the measurement errors to be negligible, we estimate that we could resolve year-to-year changes of 1.4 Sv $[(3.0^2/9 \times 2)^{1/2}]$ and 0.6 Sv $[(4.2^2/90 \times 2)^{1/2}]$ for decade-to-decade changes.

For $U_{WB5\text{-}EAST}$, the western endpoint of the zonal transport integration is located east of the western boundary of the Antilles current system (Johns et al. 2008) and therefore it may be taken as a measure of the wind-driven subtropical gyre at 26.5°N. Due to much larger and longer-period transport variations in $U_{WB5\text{-}EAST}$ compared to U_{MO}, only changes exceeding 6.2 Sv on interannual time scales and 2.2 Sv on decadal time scales can likely be resolved. It seems probable that year-to-year changes in $U_{WB5\text{-}EAST}$ are dominated by eddy noise, which may mask interannual changes in the Sverdrup gyre.

b. *Eddy contribution to the meridional overturning circulation estimated from an eddy resolving numerical model*

Figure 14 shows AMOC (U_{MO} plus Ekman plus Gulf Stream) variations at 26°N from 1988 through 2004 from an integration of the 1/12° Ocean Circulation and Climate Advanced Modelling Project (OCCAM) ocean general circulation model that is driven by realistic wind and buoyancy forcings (Marsh et al. 2009). The 30-day low-pass-filtered time series (black line) displays fluctuations of 3.0 Sv RMS.

In the subtropical North Atlantic, it is assumed that the meridional coherence scale of the zonal wind stress

exceeds 100 km (Josey et al. 2002) and that eddy-related density signals exhibit decorrelation scales of several tens of kilometers. We also expect the buoyancy-driven AMOC signal to have a meridional coherence exceeding 100 km. Therefore, the difference between AMOC fluctuations between 26° and 27°N likely reflects the influence of eddies on each section and it amounts to 1.5 Sv RMS (blue line in Fig. 14). For 365-day low-pass-filtered values (red line in Fig. 14), the variability in the AMOC difference goes down to 0.9 Sv. Thus, there is nothing reminiscent of pronounced interannual eddy-related variability in the AMOC in this model.

The small eddy contribution to the AMOC variability found in the OCCAM model is consistent with the results from Biastoch et al. (2008), who show that eddies only leave a small imprint on the AMOC at 26.5°N in their $^1/_{12}$° model. Other eddy-permitting models also exhibit a decrease of the SSH variability close to the western boundary (e.g., Hurlburt and Hogan 2000; Maltrud and McClean 2005) and therefore suggest an attenuation of the eddy variability at the western boundary itself, in agreement with the observations presented in this study (Fig. 6).

c. AMOC monitoring using altimetry?

Within 100 km of the western boundary, there is a rapid westward reduction in the variance of the upper-ocean transport that is explained by the linear regression to the zonal η difference [$U_{\mathrm{WBX\text{-}EAST}} = (\eta_{\mathrm{EAST}} - \eta_{\mathrm{WBX}}) * s_{\mathrm{WBX}}$]. This finding is in line with the results of Hirschi et al. (2009), who studied the problem using an eddy-permitting numerical model. In their model simulation, η is available at each grid point, and in the model η near the coast is not degraded by land effects. The agreement between the observations and the numerical modeling strengthens the argument that there is a dynamical reason for the failure of the relationship between the boundary-to-boundary gradients in η and U_{MO}. For the relationship to fail means that no stable (i.e., time invariant) relationship between surface geostrophic flows (as measured by the gradient in η) and U_{MO} exists. The gradual loss of this relationship, as the western endpoint approaches the boundary, has been shown from our mode analysis to be due to a gradual increase in the importance of the second mode (at the expense of the first mode). For the second mode the surface geostrophic transport has the opposite sign of that of the depth-integrated upper-ocean transport. We speculate that this is a result of (i) complicated mixed barotropic–baroclinic flow over sloping bathymetry (Bryden et al. 2009, manuscript submitted to *Ocean Sci. Discuss.*), (ii) the gradual suppression of the eddy variability, and (iii) the more pronounced influence of coastally trapped waves near the boundary.

More sophisticated methods of using η to infer U_{MO} (or the strength of the AMOC) should be tested, as the benefit of a successful technique would be high: we could establish a relationship to derive a continuous time series of the AMOC at 26.5°N from the starting point of the TOPEX/Poseidon mission in 1992, given that daily estimates of Gulf Stream transport and Ekman transport are also available for this period.

Model simulations seem to imply that the observed pronounced multidecadal variations of sea surface temperature over the North Atlantic (e.g., Mann et al. 1995) are directly linked to changes in the strength of the AMOC (Latif et al. 2004; Knight et al. 2005). While observational evidence for this link is missing because a reliable AMOC time series spanning several decades does not exist, it is possible that on multidecadal time scales η averaged over the North Atlantic may serve as a proxy for AMOC variations.

The 0.3° resolution of the gridded Aviso dataset may represent a practical limitation of the altimetry in estimating the rapid westward decrease in η over 100 km. Measurements near the coast have to be viewed with caution, as standard tidal and atmospheric corrections may have larger errors than offshore, and faster and smaller-scale dynamics than encountered in the open ocean might add additional challenges to the interpretation of coastal data (Bouffard et al. 2008). However, we interpret the finding that the RMS variability in η at mooring site WB2 is in agreement with the density observations as a strong indication that η is not particularly affected by the these problems at this location.

7. Summary

The main results of this study can be summarized as follows. The meridional upper midocean transport U_{MO} integrated between Morocco and the Bahamas varies by 3.0 Sv RMS between April 2004 and October 2006. Zonally integrated upper-ocean transports between Morocco and stations 16, 40, and 500 km off the shelf of the Bahamas show fluctuations of 3.6, 6.0, and 10.8 Sv RMS, respectively, and thus exceed those of U_{MO}. In agreement with that, both the mooring and altimetric measurements of sea surface height variability show a threefold decline within roughly 100 km of (and toward) the shelf of the Bahamas. The findings imply that in order to capture the variability of U_{MO} (and the AMOC) reliable in situ density measurements need to be taken right at the ocean boundaries.

There is a gradual decrease in the correlation between upper-ocean transport (integrated between the eastern boundary and different sites within 500 km of the western boundary) and the difference in η between the

corresponding section endpoints, as the western endpoint moves westward. The correlation coefficient drops from 0.85, for a station located 500 km offshore, to a statistically insignificant value of only 0.12 for the basinwide integration. We consider the gradual decrease in correlation, as the western section endpoint is moved westward, to be mainly a consequence of changes in the vertical structure of the integrated flow, because of flow reversals in the upper 1000 m becoming increasingly important over the continental slope compared to offshore conditions. The results imply that the basinwide difference of η does not provide reliable estimates of the temporal evolution of U_{MO}.

The nonlinear reduced-gravity model used to study eddy–boundary interaction is able to reproduce both the observed decline in the amplitude of η within 100 km from the western boundary and the corresponding reduction in the integrated transport fluctuations. It shows that eddies impinging on the western boundary kick off fast boundary waves that propagate equatorward and account for the observed decline.

An analytical linear model based on a simple budget of incoming long and reflected short Rossby waves at the western boundary provides a scaling for the reduction of thermocline thickness (or η) on the western boundary compared to offshore conditions according to $f/(\beta\Delta y)$. At 26.5°N and for a meridional scale, $\Delta y = 500$ km of the incoming wave yields a decrease by a factor of 6.

Physically, this amplitude reduction occurs because an along-boundary pressure gradient cannot be maintained by a Coriolis force (since there cannot be flow into the boundary). Instead a fluid acceleration is generated, which rapidly propagates any pressure anomalies along the boundary.

Overall, our results suggest that the local eddy field does not have the potential to dominate AMOC variability at 26.5°N on interannual to decadal time scales. If a monitoring system based on boundary-to-boundary density gradient observations can be maintained in the ocean continuously over climate relevant time scales, it will document the temporal evolution of the strength of the AMOC, whether it be random fluctuations, regular oscillations, or a long-term trend.

Acknowledgments. The authors thank the captains and crews of the Research Vessels *Charles Darwin*, *Discovery*, *Ronald H. Brown*, *Knorr*, *Poseidon*, and *Seward Johnson*, and the UKORS and RSMAS mooring teams. The mooring operations have been funded through NERC RAPID and NSF. The altimetric data used in this study have kindly been made available by AVISO (information online at http://www.aviso.oceanobs.com). The Florida Current cable data are made freely available by the Atlantic Oceanographic and Meteorological Laboratory (information online at www.aoml.noaa.gov/phod/floridacurrent/) and are funded by the NOAA Office of Climate Observations. The wind stress data were obtained from CERSAT, at IFREMER, Plouzané, France. We thank Darren Rayner (NOCS) for coordinating and planning the seagoing activities and leading the mooring data recovery. The competent help from Julie Collins and John Molina in processing the mooring data is highly appreciated. The OCCAM MOC time series has been made available to us by Bob Marsh. Two of the authors (TK, JJMH) were supported within the framework of the NERC-funded Rapid Climate Change Programme (Grant NER/T/S/2002/00481). HLJ is funded by a Royal Society University research fellowship, for which she is grateful.

REFERENCES

Baringer, M. O., and J. C. Larsen, 2001: Sixteen years of Florida Current transport at 27°N. *Geophys. Res. Lett.,* **28,** 3179–3182.

Beal, L. M., and H. L. Bryden, 1999: The velocity and vorticity structure of the Agulhas Current at 32S. *J. Geophys. Res.,* **104,** 5151–5176.

Beckmann, A., 1988: Vertical structure of midlatitude mesoscale instabilities. *J. Phys. Oceanogr.,* **18,** 1354–1371.

Biastoch, A., C. W. Böning, and J. Getzlaff, 2008: Causes of interannual–decadal variability in the Meridional Overturning Circulation of the midlatitude North Atlantic Ocean. *J. Climate,* **21,** 6599–6615.

Bouffard, J., S. Vignudelli, P. Cipollini, and Y. Menard, 2008: Exploiting the potential of an improved multimission altimetric data set over the coastal ocean. *Geophys. Res. Lett.,* **35,** L10601, doi:10.1029/2008GL033488.

Bryden, H. L., W. E. Johns, and P. M. Saunders, 2005: Deep Western Boundary Current east of Abaco: Mean structure and transport. *J. Mar. Res.,* **63,** 35–57.

Chelton, D. B., M. G. Schlax, R. M. Samelson, and R. A. de Szoeke, 2007: Global observations of large oceanic eddies. *Geophys. Res. Lett.,* **34,** L15606, doi:10.1029/2007GL030812.

Clarke, A. J., and C. Shi, 1991: Critical frequencies at ocean boundaries. *J. Geophys. Res.,* **96,** 10 731–10 738.

Cunningham, S. A., and M. Pavic, 2007: A time series of surface geostrophic currents across the Antarctic Circumpolar Current in Drake Passage. *Prog. Oceanogr.,* **73,** 296–310.

——, and Coauthors, 2007: Temporal variability of the Atlantic Meridional Overturning Circulation at 26.5°N. *Science,* **317,** 935–938.

Cushman-Roisin, B., 1994: *Introduction to Geophysical Fluid Dynamics*. Prentice-Hall, 320 pp.

Dibarboure, G., O. Lauret, F. Mertz, and V. Rosmorduc, 2008: SSALTO/DUACS user handbook: (M)SLA and (M)ADT near-real time and delayed time products. CLS-DOS-NT-06.034, SALP-MU-P-EA-21065-CLS, Issue 1, Rev. 9, Aviso User Service, Ramonville St-Agne, France, 41 pp. [Available online at www.aviso.oceanobs.com/fileadmin/documents/data/tools/hdbk_duacs.pdf.]

Fu, L.-L., and G. Pihos, 1994: Determining the response of sea level to atmospheric pressure forcing using TOPEX/POSEIDON data. *J. Geophys. Res.,* **99,** 24 633–24 642.

Hallberg, R., and P. Rhines, 1996: Buoyancy-driven circulation in an ocean basin with isopycnals intersecting the sloping boundary. *J. Phys. Oceanogr.,* **26,** 913–940.

Hirschi, J. J.-M., P. D. Killworth, J. R. Blundell, and D. Cromwell, 2009: Sea surface heights signal as indicators for oceanographic meridional mass transports. *J. Phys. Oceanogr.,* **39,** 581–601.

Hurlburt, H. E., and P. J. Hogan, 2000: Impact of 1/8° to 1/64° resolution on Gulf Stream model–data comparisons in basin-scale subtropical Atlantic Ocean models. *Dyn. Atmos. Oceans,* **32,** 283–329.

Huthnance, J. M., 1978: On coastal trapped waves: Analysis and numerical calculation by inverse iteration. *J. Phys. Oceanogr.,* **8,** 74–92.

Johns, W. E., and D. R. Watts, 1986: Times scales and structure of topographic Rossby waves and meanders in the deep Gulf Stream. *J. Mar. Res.,* **44,** 267–290.

——, T. N. Lee, D. X. Zhang, R. Zantopp, C. T. Liu, and Y. Yang, 2001: The Kuroshio east of Taiwan: Moored transport observations from the WOCE PCM-1 array. *J. Phys. Oceanogr.,* **31,** 1031–1053.

——, T. Kanzow, and R. Zantopp, 2005: Estimating ocean transports with dynamic height moorings: An application in the Atlantic Deep Western Boundary Current. *Deep-Sea Res. I,* **52,** 1542–1567.

——, L. M. Beal, M. O. Baringer, J. R. Molina, S. A. Cunningham, T. Kanzow, and D. Rayner, 2008: Variability of Shallow and Deep Western Boundary Currents off the Bahamas during 2004–05: Results from the 26°N RAPID–MOC array. *J. Phys. Oceanogr.,* **38,** 605–623.

Johnson, H. L., and D. P. Marshall, 2002: A theory for the surface Atlantic response to thermohaline variability. *J. Phys. Oceanogr.,* **32,** 1121–1132.

Josey, S. A., E. C. Kent, and P. K. Taylor, 2002: On the wind stress forcing of the ocean in the SOC climatology: Comparisons with the NCEP–NCAR, ECMWF, UWM/COADS, and Hellerman and Rosenstein datasets. *J. Phys. Oceanogr.,* **32,** 1993–2019.

Kanzow, T., U. Send, W. Zenk, A. D. Chave, and M. Rhein, 2006: Monitoring the integrated deep meridional flow in the tropical North Atlantic: Long-term performance of a geostrophic array. *Deep-Sea Res. I,* **53,** 528–546.

——, and Coauthors, 2007: Flow compensation associated with the MOC at 26.5°N in the Atlantic. *Science,* **317,** 938–941.

——, U. Send, and M. McCartney, 2008a: On the variability of the deep meridional transports in the tropical North Atlantic. *Deep-Sea Res. I,* **55,** 1601–1623, doi:10.1016/j.dsr.2008.07.011.

——, and Coauthors, 2008b: A prototype system for observing the Atlantic Meridional Overturning Circulation—Scientific basis, measurement and risk mitigation strategies, and first results. *J. Operational Oceanogr.,* **1,** 19–28.

Knight, J. R., R. J. Allan, C. K. Folland, M. Vellinga, and M. E. Mann, 2005: A signature of persistent natural thermohaline circulation cycles in observed climate. *Geophys. Res. Lett.,* **32,** L20708, doi:10.1029/2005GL024233.

Latif, M., and Coauthors, 2004: Reconstructing, monitoring, and predicting multidecadal-scale changes in the North Atlantic thermohaline circulation with sea surface temperature. *J. Climate,* **17,** 1605–1614.

Lee, T. N., W. Johns, F. Schott, and R. Zantopp, 1990: Western boundary current structure and variability east of Abaco, Bahamas, at 26.5°N. *J. Phys. Oceanogr.,* **20,** 446–466.

——, ——, R. J. Zantopp, and E. R. Fillenbaum, 1996: Moored observations of western boundary current variability and thermocline circulation at 26.5°N in the subtropical North Atlantic. *J. Phys. Oceanogr.,* **26,** 962–983.

Maltrud, M. E., and J. L. McClean, 2005: An eddy resolving global 1/10° ocean simulation. *Ocean Modell.,* **8,** 31–54, doi:10.1016/j.ocemod.2003.12.001.

Mann, M. E., J. Park, and R. S. Bradley, 1995: Global interdecadal and century-scale climate oscillations during the past 5 centuries. *Nature,* **378,** 266–270.

Marsh, R., B. A. de Cuevas, A. C. Coward, J. Jacquin, J. J.-M. Hirschi, and S. A. Josey, 2009: Recent changes in the North Atlantic circulation simulated with eddy-permitting and eddy-resolving ocean models. *Ocean Modell.,* **28,** 226–239.

McPhaden, M. J., and D. Zhang, 2002: Slowdown of the meridional overturning circulation in the upper Pacific Ocean. *Nature,* **415,** 603–608.

Minato, S., 1982: Geostrophic adjustment near the coast. *J. Oceanogr. Soc. Japan,* **38,** 225–235.

MODE Group, 1978: The Mid-Ocean Dynamics Experiment. *Deep-Sea Res.,* **25,** 859–910.

MODE-1 Atlas Group, 1977: *Atlas of the Mid-Ocean Dynamics Experiment (MODE-1)*. Massachusetts Institute of Technology, Cambridge, MA, 274 pp.

Nof, D., 1988: Eddy–wall interactions. *J. Mar. Res.,* **46,** 527–555.

O'Rourke, E. A., 2009: The effect of topography on thermohaline adjustment. Ph.D. thesis, University of Liverpool, 189 pp.

Richman, J. G., C. Wunsch, and N. G. Hogg, 1977: Space and time scales of mesoscale motions in the western North Atlantic. *Rev. Geophys. Space Phys.,* **15,** 385–420.

Sato, O. T., and T. Rossby, 1995: Seasonal and low frequency variations in dynamic height anomaly and transport of the Gulf Stream. *Deep-Sea Res. I,* **42,** 149–164.

Schmittner, A., M. Latif, and B. Schneider, 2005: Model projections of the North Atlantic thermohaline circulation for the 21st century assessed by observations. *Geophys. Res. Lett.,* **32,** L23710, doi:10.1029/2005GL024368.

Stammer, D., 1997: Global characteristics of ocean variability from regional TOPEX/POSEIDON altimeter measurements. *J. Phys. Oceanogr.,* **27,** 1743–1769.

Watts, D. R., and H. Kontoyiannis, 1990: Deep-ocean bottom pressure measurement: Drift removal and performance. *J. Atmos. Oceanic Technol.,* **7,** 296–306.

Whitworth, T., III, 1983: Monitoring the transport of the Antarctic circumpolar current at Drake Passage. *J. Phys. Oceanogr.,* **13,** 2045–2057.

Wijffels, S. E., 2001: Ocean transport of fresh water. *Ocean Circulation and Climate: Observing and Modelling the Global Ocean,* G. Siedler, J. Church, and J. Gould, Eds., Academic Press, 475–488.

Woodgate, R. A., and K. Aagaard, 2005: Revising the Bering Strait freshwater flux into the Arctic Ocean. *Geophys. Res. Lett.,* **32,** L02602, doi:10.1029/2004/GL021747.

Wunsch, C., 1997: The vertical partition of oceanic horizontal kinetic energy. *J. Phys. Oceanogr.,* **27,** 1770–1794.

——, 2008: Mass and volume transport variability in an eddy-filled ocean. *Nature Geosci.,* **1,** 165–168, doi:10.1038/ngeo126.

——, and D. Stammer, 1998: Satellite altimetry, the marine geoid, and the oceanic general circulation. *Annu. Rev. Earth Planet. Sci.,* **26,** 219–253.